

This is an Open Access document downloaded from ORCA, Cardiff University's institutional repository: <https://orca.cardiff.ac.uk/id/eprint/167991/>

This is the author's version of a work that was submitted to / accepted for publication.

Citation for final published version:

Chachvalvutikul, Auttaphon, Luangwanta, Tawanwit, Inceesungvorn, Burapat and Kaowphong, Sulawan 2023. Bismuth-rich oxyhalide (Bi₇O₉I₃?Bi₄O₅Br₂) solid-solution photocatalysts for the degradation of phenolic compounds under visible light. *Journal of Colloid and Interface Science* 641 , pp. 595-609.
10.1016/j.jcis.2023.03.063

Publishers page: <http://dx.doi.org/10.1016/j.jcis.2023.03.063>

Please note:

Changes made as a result of publishing processes such as copy-editing, formatting and page numbers may not be reflected in this version. For the definitive version of this publication, please refer to the published source. You are advised to consult the publisher's version if you wish to cite this paper.

This version is being made available in accordance with publisher policies. See <http://orca.cf.ac.uk/policies.html> for usage policies. Copyright and moral rights for publications made available in ORCA are retained by the copyright holders.



Bismuth-rich oxyhalide ($\text{Bi}_7\text{O}_9\text{I}_3\text{-Bi}_4\text{O}_5\text{Br}_2$) solid-solution photocatalysts for the degradation of phenolic compounds under visible light

Auttaphon Chachvalvutikul^a, Tawanwit Luangwanta^a, Burapat Inceesungvorn^{a,b,c}, Sulawan Kaowphong^{a,b,c*}

^a Department of Chemistry, Faculty of Science, Chiang Mai University, Chiang Mai 50200, Thailand

^b Center of Excellence in Materials Science and Technology, Chiang Mai University, Chiang Mai 50200, Thailand

^c Materials Science Research Center, Faculty of Science, Chiang Mai University, Chiang Mai 50200, Thailand

* Corresponding author

E-mail address: sulawank@gmail.com, sulawan.k@cmu.ac.th

Tel: +66 53 943341

Fax: +66 53 892277

Abstract

Hypothesis The development of solid-solution photocatalysts with tunable bandgaps and band structures, which are significant factors that influence their photocatalytic properties, is crucial.

Experiments We fabricated a series of novel bismuth-rich $\text{Bi}_7\text{O}_9\text{I}_3\text{-Bi}_4\text{O}_5\text{Br}_2$ solid-solution photocatalysts with controlled I:Br molar ratios (denoted as $\text{B-I}_x\text{Br}_{1-x}$, $x = 0.2, 0.3, 0.4, \text{ or } 0.6$) via a rapid, facile, and energy-efficient microwave-heating route. The photodegradations under visible-light irradiation of the phenolic compounds (4-nitrophenol (4NP), 3-nitrophenol (3NP), and bisphenol A (BPA)), and the simultaneous photodegradation of BPA and rhodamine B (RhB) in a coexisting BPA–RhB system were investigated.

Findings The $\text{B-I}_{0.3}\text{Br}_{0.7}$ solid solution provided the highest photocatalytic activity toward 4NP degradation, with degradation rates 32 and 4 times higher than those of $\text{Bi}_7\text{O}_9\text{I}_3$ and $\text{Bi}_4\text{O}_5\text{Br}_2$, respectively. The photodegradation efficiency of the studied phenolic compounds followed the order $\text{BPA (97.5\%)} > \text{4NP (72.8\%)} > \text{3NP (27.5\%)}$. The RhB-sensitization mechanism significantly enhanced the photodegradation efficiency of BPA. Electrochemical measurements demonstrated the efficient separation and migration of charge carriers in the $\text{B-I}_{0.3}\text{Br}_{0.7}$ solid solution, which enhanced the photocatalytic activity. The $\text{B-I}_{0.3}\text{Br}_{0.7}$ solid solution effectively activated molecular oxygen to produce $\cdot\text{O}_2^-$, which subsequently produced other reactive species, including H_2O_2 and $\cdot\text{OH}$, as revealed by reactive-species trapping, nitroblue tetrazolium transformation, and o-tolidine oxidation experiments.

Keywords: Bismuth-rich oxyhalide; Solid solution; Dye-sensitization; Photodegradation; Phenolic compounds; Microwave synthesis

1. Introduction

Over the last few decades, urbanization and industrialization have developed at an unprecedented rate, resulting in an increase in water consumption and the release of wastewater into the environment. Colorless organic pollutants, particularly phenolic compounds, are commonly found in industrial effluents [1]. These compounds cannot be degraded naturally because of their high stability against chemical and biological degradation processes [2–8]. This limits water usage and threatens human health even at low concentrations. For example, carcinogenic and mutagenic nitrophenols are classified as major pollutants by the Agency for Toxic Substances and Disease Registry (ATSDR) and Environmental Protection Agency (EPA), with a restricted concentration of 10 ppb in water [9,10]. In addition, bisphenol A, a typical endocrine-disrupting chemical commonly used in plastic manufacture, has been proven to have estrogenic activity even at concentrations below $1 \mu\text{g m}^{-3}$ [11].

Photoactive-semiconductor-based heterogeneous photocatalysis has been considered a promising technology for the degradation of phenolic contaminants in wastewater using sunlight or artificial light sources [12,13]. The development of semiconductor photocatalysts with high energy-harvesting capabilities has attracted significant attention. Among the widely studied semiconductor photocatalysts, bismuth oxyhalides (BiOX ; $\text{X} = \text{Cl, Br, I}$) have received significant attention because their unique layered structure, consisting of $[\text{X-Bi-O-Bi-X}]$ slabs, can simulate an internal electric field (IEF) along the crystal orientation perpendicular to the $[\text{Bi}_2\text{O}_2]$ and halogen layers. The generated IEF is expected to facilitate the separation and migration of photogenerated electron–hole pairs [14]. However, practical applications of BiOX materials are still limited by their poor light-absorption abilities and photocatalytic oxidation/reduction properties, the high recombination probability of photogenerated electron–hole pairs, and

ineffective photogenerated charge transfer to the photocatalyst surface [15]. Overcoming these drawbacks is a major concern [12]. Because the maximum valence band (VB) of BiOX primarily comprises O 2*p* and X *np* orbitals (*n* = 3, 4, and 5 for X = Cl, Br, and I, respectively), whereas the minimum conduction band (CB) is dominated by Bi 6*p* orbitals, the VB and CB edge alignments and energy bandgaps of BiOX can be modulated via layered-structure engineering by removing the halogen ions that are weakly bound by van der Waals interactions, essentially enriching the Bi content in the crystal structure [16,17]. Increasing the Bi-to-X ratio enhances the photon-absorption efficiency and the hybridization of the CB to promote electron migration and photogenerated-charge-separation efficiency [15]. Consequently, the visible-light absorption and photocatalytic oxidation/reduction properties of the bismuth-rich (dehalogenated) Bi_{*x*}O_{*y*}X_{*z*} compounds can be improved over those of ordinary BiOX materials. Various bismuth-rich Bi_{*x*}O_{*y*}X_{*z*} photocatalysts have been developed to improve the photocatalytic performance of ordinary BiOX. For instance, Bi₄O₅I₂ and Bi₇O₉I₃ show higher photocatalytic activities toward the degradation of rhodamine B [18], phenol [18–20], and 4-*tert*-butylphenol [21] than BiOI. Bi₅O₇Br and Bi₄O₅Br₂ exhibit higher visible-light-driven photocatalytic activities than BiOBr for the degradation of bisphenol A [22–24] and resorcinol [25,26].

A solid-solution approach has also been employed to enhance the energy-utilization efficiencies and redox properties of BiOX photocatalysts. Accurately controlling the compositions of various halides can tune the energy bandgap and band-edge potential, and regulate charge separation and migration. However, the preparation of solid solutions has been limited to stoichiometric BiOX compounds such as BiOCl_{*x*}I_{1-*x*}, BiOBr_{*x*}I_{1-*x*}, and BiOCl_{*x*}Br_{1-*x*} [27–30]. Recently, enhanced photocatalytic properties of solid solutions of bismuth-rich Bi_{*x*}O_{*y*}X_{*z*} have been reported [12,17,31,32]. For example, compared with Bi₄O₅Br₂ and Bi₄O₅I₂ as photocatalysts,

$\text{Bi}_4\text{O}_5\text{BrI}$ solid solutions exhibit superior photocatalytic activities for CO_2 photoconversion and Cr(VI) photoreduction [17], and in their photooxidation ability for phenol and rhodamine B degradation [12]. $\text{Bi}_3\text{O}_4\text{Cl}_{0.5}\text{Br}_{0.5}$ solid solution can remove 60% of NO in 10 min under visible-light irradiation with a higher degradation rate than that of pure $\text{Bi}_3\text{O}_4\text{Cl}$ and $\text{Bi}_3\text{O}_4\text{Br}$ [31]. The $\text{Bi}_5\text{O}_7\text{Br}_{0.5}\text{I}_{0.5}$ solid solution shows a higher photocatalytic efficiency for oilfield-wastewater treatment than $\text{Bi}_5\text{O}_7\text{Br}$ or $\text{Bi}_5\text{O}_7\text{I}$ and displays universal photocatalytic activity for the degradation of rhodamine B, phenol, and bisphenol A [32]. However, the syntheses of both bismuth-rich $\text{Bi}_x\text{O}_y\text{X}_z$ and their solid solutions require complicated synthetic steps [17,32], harsh reaction conditions [31], and long reaction times [12,17,32]. Therefore, developing a facile and cost-effective synthetic approach to exploring novel bismuth-rich $\text{Bi}_x\text{O}_y\text{X}_z$ solid-solution photocatalysts with enhanced photocatalytic performance is a challenge. To date, microwave heating method has been applied to synthesize bismuth-rich $\text{Bi}_x\text{O}_y\text{X}_z$ [33–35] because of several advantages over the conventional heating methods, such as rapid volumetric heating, savings in energy and time, fast crystallization kinetics, and homogeneous nucleation of the materials [36].

Recently, we successfully synthesized bismuth-rich $\text{Bi}_7\text{O}_9\text{I}_3$ and $\text{Bi}_4\text{O}_5\text{Br}_2$ photocatalysts using microwave heating, which is a rapid, facile, environmentally friendly, and single-step method [37,38]. Using microwave irradiation, highly crystalline $\text{Bi}_7\text{O}_9\text{I}_3$ and $\text{Bi}_4\text{O}_5\text{Br}_2$ nanostructures were obtained over short periods (30 and 55 min for $\text{Bi}_7\text{O}_9\text{I}_3$ and $\text{Bi}_4\text{O}_5\text{Br}_2$, respectively). The outcomes of our previous studies and the aforementioned reports motivated us to employ the synergistic effects of bismuth-rich solid solutions for the degradation of phenolic compounds to improve the photocatalytic performances of $\text{Bi}_7\text{O}_9\text{I}_3$ and $\text{Bi}_4\text{O}_5\text{Br}_2$. In the present work, we first synthesized a series of bismuth-rich $\text{Bi}_7\text{O}_9\text{I}_3$ – $\text{Bi}_4\text{O}_5\text{Br}_2$ ($\text{B-I}_x\text{Br}_{1-x}$) solid solutions with various I:Br molar ratios using a microwave irradiation method. The optimal I:Br ratio in the

$\text{Bi}_x\text{Br}_{1-x}$ solid solution was determined by the photocatalytic degradation of a 4-nitrophenol (4NP) solution under visible-light irradiation. The $\text{Bi}_7\text{O}_9\text{I}_3$ – $\text{Bi}_4\text{O}_5\text{Br}_2$ solid solution with an I:Br molar ratio of 0.3:0.7 afforded the highest photodegradation efficiency under visible-light irradiation and at a higher rate than the $\text{Bi}_7\text{O}_9\text{I}_3$ and $\text{Bi}_4\text{O}_5\text{Br}_2$ parent materials. The photocatalyst also exhibited universality for the degradation of other phenolic compounds, including 3-nitrophenol (3NP) and bisphenol A (BPA). A possible photocatalytic mechanism for 4NP degradation using this solid-solution photocatalyst was revealed via reactive-species trapping experiments, nitroblue tetrazolium (NBT) transformation, *o*-tolidine oxidation, and the terephthalic acid photoluminescence (TA-PL) probing technique. The simultaneous photodegradation of the combined pollution systems of selected phenolic compounds with rhodamine B (RhB) dye was also revealed.

2. Materials and methods

2.1. Preparation of the $\text{Bi}_7\text{O}_9\text{I}_3$, $\text{Bi}_4\text{O}_5\text{Br}_2$, and $\text{Bi}_7\text{O}_9\text{I}_3$ – $\text{Bi}_4\text{O}_5\text{Br}_2$ solid solutions

To prepare the $\text{Bi}_7\text{O}_9\text{I}_3$ and $\text{Bi}_4\text{O}_5\text{Br}_2$ powders, $\text{Bi}(\text{NO}_3)_3 \cdot 5\text{H}_2\text{O}$ (1 mmol; Sigma-Aldrich, $\geq 95\%$) was dissolved in 30 mL of ethylene glycol (Carlo Erba Reagents, 99.5%). A solution of KI or KBr (1 mmol; Sigma-Aldrich, 99%) in ethylene glycol (10.0 mL) was added to the $\text{Bi}(\text{NO}_3)_3 \cdot 5\text{H}_2\text{O}$ solution and stirred vigorously for 30 min. Next, the mixed solution was placed in a microwave oven (2450 MHz-EMS28205, Electrolux, China) and irradiated at 600 W for 110 cycles, where one cycle was ‘on’ for 30 s and ‘off’ for 60 s. The powder obtained was washed several times with deionized water and ethanol, collected via filtration, and finally dried in an oven at 70 °C.

The procedure for the preparation of the $\text{Bi}_7\text{O}_9\text{I}_3\text{-Bi}_4\text{O}_5\text{Br}_2$ solid solutions was the same as that for $\text{Bi}_7\text{O}_9\text{I}_3$ and $\text{Bi}_4\text{O}_5\text{Br}_2$; however, a mixture of KI and KBr (a total of 1 mmol) was used. The $\text{Bi}_7\text{O}_9\text{I}_3\text{-Bi}_4\text{O}_5\text{Br}_2$ solid-solution samples were labeled as $\text{B-I}_x\text{Br}_{1-x}$, where $x = 0.2, 0.3, 0.4,$ or 0.6 .

2.2. Characterization

The composition, phase, and structure of the as-prepared powders were examined by X-ray diffraction (XRD) spectroscopy using an X-ray diffractometer (Rigaku Smartlab). The microstructures and morphologies of the samples were investigated using field-emission scanning electron microscopy (SEM, JEOL JSM-6335F) and transmission electron microscopy (TEM, JEOL JEM-2010). The elemental compositions were determined using a scanning electron microscope equipped with an energy dispersive X-ray spectroscope (SEM-EDS). The elemental distribution mappings were observed using a scanning TEM-EDS. The surface compositions were analyzed using X-ray photoelectron spectroscopy (XPS, AXIS Ultra DLD, Kratos Analytical Ltd.) with an Al $K\alpha$ X-ray source. UV-Vis diffuse-reflectance spectra were recorded (UV-Vis DRS, UV-1800 Shimadzu) using BaSO_4 as the reference material. The specific surface area was investigated by N_2 adsorption at $-196\text{ }^\circ\text{C}$ using a Quantachrome instrument and calculated using the Brunauer-Emmett-Teller (BET) method. Prior to the analysis, the samples were degassed at $120\text{ }^\circ\text{C}$ for 3 h under vacuum. Inductively coupled plasma mass spectrometry (ICP-MS) was used to determine the concentrations of I and Br in the $\text{B-I}_x\text{Br}_{1-x}$ solid-solution samples. Before analysis, the sample powder was completely dissolved in nitric acid solution [39], and the analysis was then performed on Shimadzu's ICPMS-2030 using the analytical conditions and ICP-MS parameters provided in the Supporting Information.

The electrochemical properties were examined on a potentiostat/galvanostat electrochemical work-station (Autolab PGSTAT128N, Metrohm Siam Ltd.) equipped with a three-electrode configuration system using Na₂SO₄ aqueous solution (0.5 M, pH = 5.0) as the electrolyte. A platinum wire and a commercial Ag/AgCl (3.0 M KCl) electrode were used as the counter and reference electrodes, respectively. To fabricate the working electrode, the synthesized powder was dispersed in isopropanol and sonicated for 5 min. Subsequently, the dispersion was deposited on a fixed area (1 cm²) of a fluorine-doped tin oxide (FTO)-coated glass substrate, which was dried at room temperature for 1 h. Electrochemical impedance spectroscopy (EIS) was performed in the frequency range of 10⁵ to 10⁻¹ Hz, with an amplitude of 0.05 V at a bias potential of 1.50 V in the dark. Mott–Schottky plots were recorded at a frequency of 10 Hz, without an external bias. Linear sweep voltammetry (LSV) was performed in an applied potential range of 0–2.0 V, with a scan rate of 50 mV s⁻¹. The transient photocurrent response was recorded at an applied potential of 1.0 V, using two 50 W white LED lamps to irradiate the front and back of the working electrode.

2.3. Photocatalytic degradation of phenolic compounds

A suspension of the photocatalyst (100 mg) in 4NP solution (10 ppm; Sigma-Aldrich, ≥99%) was stirred for 30 min in the dark to establish an adsorption–desorption equilibrium on its surface, and then exposed to visible light (50 W LED lamp). At regular time intervals, 2.5 mL of the suspension was sampled, and the photocatalyst powder was separated by centrifugation. The concentration of the remaining 4NP was determined using a UV–Vis spectrophotometer (UV-1800, Shimadzu) at its characteristic absorption wavelength of 318 nm. In addition, the photodegradation of 3NP (Sigma-Aldrich, ≥99%) and BPA (Sigma-Aldrich, ≥99%) was carried

out at the same concentration (10 ppm) under the same photocatalytic conditions, and the centrifuged solutions were analyzed for 3NP and BPA by measuring the absorbance at characteristic wavelengths of 273 and 277 nm, respectively. The photodegradation efficiency (%DE) and pseudo-first order kinetics were calculated using the following equations:

$$\%DE = \frac{A_0 - A}{A_0} \times 100 \quad (1)$$

$$\ln\left(\frac{A_0}{A}\right) = k_{app}t \quad (2)$$

where A_0 and A represent the concentrations of the organic pollutant after the surface of the photocatalyst had reached adsorption–desorption equilibrium and after light irradiation, respectively, and k_{app} and t represent the apparent rate constant (min^{-1}) and reaction time (min), respectively. The phenolic compounds were also photolyzed under the same experimental conditions (a blank experiment).

To determine the reactive species in the photocatalytic reaction, reactive-species trapping experiments were conducted by adding $1 \times 10^{-3} \text{ mol L}^{-1}$ of various scavengers to the 4NP degradation system; p-benzoquinone (BQ; Sigma-Aldrich, $\geq 98\%$) [13], ethylenediaminetetraacetic acid disodium salt (EDTA-2Na; Sigma-Aldrich, $\geq 99\%$) [40], and isopropyl alcohol (IPA; QRëC™, $\geq 99.7\%$) [13] were added to the reaction systems to scavenge $\bullet\text{O}_2^-$, h^+ (positive hole), and $\bullet\text{OH}$, respectively. The generation of $\bullet\text{O}_2^-$ was further confirmed by monitoring the conversion of NBT ($1.5 \times 10^{-5} \text{ mol L}^{-1}$; Sigma-Aldrich, 90.0-110.0%) to a formazan derivative under visible-light irradiation [41]. Considering the reaction between NBT and $\bullet\text{O}_2^-$ in the molar ratio of 1:4 [42], the amount of $\bullet\text{O}_2^-$ was quantitatively determined by measuring the decrease in the absorbance of the NBT solution at its maximum absorption wavelength (λ_{max}) of 259 nm using the UV–Vis spectrophotometer. The formation of hydrogen

peroxide (H_2O_2) in the photocatalytic reaction was detected using *o*-tolidine ($1 \times 10^{-3} \text{ mol L}^{-1}$; Sigma-Aldrich, $\geq 95\%$) as a probe molecule to form the 2-electron oxidation product (2-electron oxidized tolidine) [43,44]; the concentration of oxidized tolidine was determined by measuring its absorbance at a λ_{max} of 446 nm using the UV–Vis spectrophotometer. The presence of $\bullet\text{OH}$ was verified using the TA-PL probing technique [45]; the evolution of the highly fluorescent 2-hydroxyterephthalic acid (TAOH; Sigma-Aldrich, 98%) was detected using a fluorescence spectrophotometer (RF-5301PC, Shimadzu) at an emission wavelength of 425 nm and an excitation wavelength of 315 nm.

3. Results and discussion

3.1. Phase and morphology

The XRD patterns of $\text{Bi}_7\text{O}_9\text{I}_3$, $\text{Bi}_4\text{O}_5\text{Br}_2$, and the $\text{B-I}_x\text{Br}_{1-x}$ solid solutions with various values of x are shown in **Fig. 1(a)**. For $\text{Bi}_7\text{O}_9\text{I}_3$, the positions of the diffraction peaks of the synthesized $\text{Bi}_7\text{O}_9\text{I}_3$ sample shifted slightly to angles smaller than those of standard tetragonal BiOI (Joint Committee of Powder Diffraction Standards (JCPDS) number 010-0445), which is in agreement with the properties of $\text{Bi}_7\text{O}_9\text{I}_3$ previously reported [46–49]. This was ascribed to the higher bismuth and oxygen contents in the BiOI lattice, which caused its structural distortion and expansion [18,47]. The diffraction peaks of the synthesized $\text{Bi}_4\text{O}_5\text{Br}_2$ sample matched well with those of standard monoclinic $\text{Bi}_4\text{O}_5\text{Br}_2$ (JCPDS number 037-0699) and those reported previously [12,41,50]. For the $\text{B-I}_x\text{Br}_{1-x}$ solid solutions, the diffraction peaks gradually shifted to larger angles with increasing Br content, as observed in the enlarged XRD patterns (**Fig. 1(b)**). This was attributed to atomic distance contraction arising from the replacement of the larger ionic radius of I^- (2.16 Å) by the smaller ionic radius of Br^- (1.96 Å) in the $\text{Bi}_7\text{O}_9\text{I}_3$ crystal lattice [27,51,52].

Notably, the XRD pattern of $B-I_{0.2}Br_{0.8}$ resembled that of $Bi_4O_5Br_2$, indicating nearly complete formation of $Bi_4O_5Br_2$. These results suggest that the synthesized $B-I_xBr_{1-x}$ were solid solutions rather than heterostructures of $Bi_7O_9I_3$ and $Bi_4O_5Br_2$ crystalline phases. No peaks arising from impurities were observed, indicating the purity of the synthesized materials.

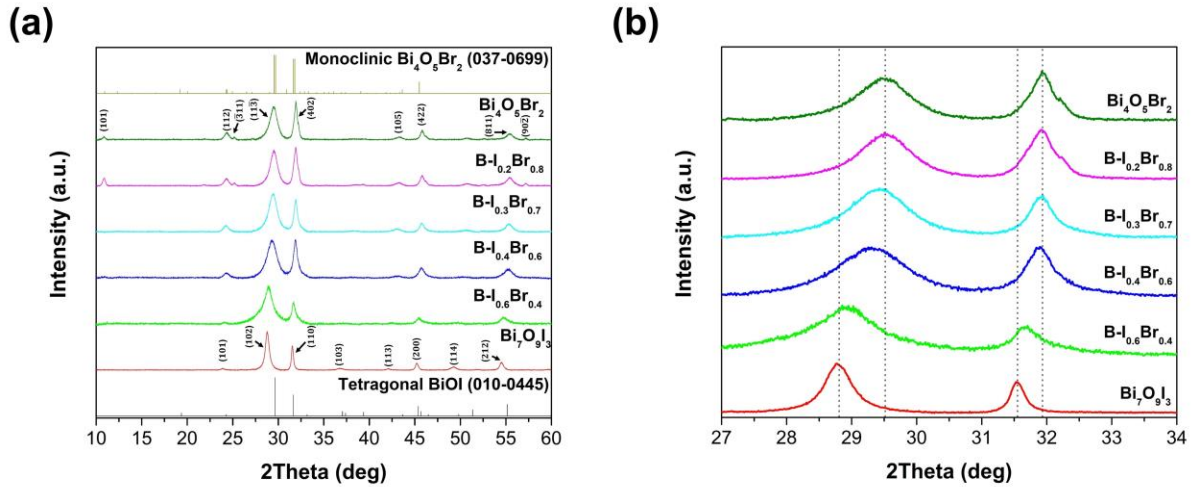


Fig. 1. (a) XRD patterns of $Bi_7O_9I_3$, $Bi_4O_5Br_2$, and $B-I_xBr_{1-x}$ solid solutions. (b) Enlarged XRD patterns between 27° and 34° .

SEM and TEM images of the $Bi_7O_9I_3$, $Bi_4O_5Br_2$, and $B-I_xBr_{1-x}$ solid solutions are shown in **Fig. 2** and **Fig. 3**, respectively. The $Bi_7O_9I_3$ powder (**Fig. 2(a)** and **Fig. 3(a)**) was composed of agglomerated nanoparticles with an average diameter of 10–20 nm. Nanoparticles with high surface-area-to-volume ratios agglomerate to minimize their surface energies. The morphologies of the $B-I_xBr_{1-x}$ solid solutions varied with the I:Br molar ratio. The SEM images of the $B-I_{0.6}Br_{0.4}$ (**Fig. 2(b)**) and $B-I_{0.4}Br_{0.6}$ (**Fig. 2(c)**) solid solutions exhibit large microsheet-like structures consisting of loosely packed thin nanoplates with many pores on their surfaces. The SEM image of the $B-I_{0.3}Br_{0.7}$ solid solution (**Fig. 2(d)**) shows micro-rod-like pieces consisting of nanosheets. Broken micro-rod-like pieces revealed their hollowness, indicated by the contrast between the dark

edges and pale centers in the TEM image (**Fig. 3(c)**). Flower-like microspheres assembled via thin nanoplates were observed for the $\text{B-I}_{0.2}\text{Br}_{0.8}$ (**Fig. 2(e)**) and $\text{Bi}_4\text{O}_5\text{Br}_2$ (**Fig. 2(f)** and **Fig. 3(b)**) samples, but the diameter of the $\text{Bi}_4\text{O}_5\text{Br}_2$ microsphere ($4.5\ \mu\text{m}$) was larger than that of the $\text{B-I}_{0.2}\text{Br}_{0.8}$ microsphere ($2.6\ \mu\text{m}$), with denser nanosheets on its surface. High-resolution TEM (HRTEM) images of $\text{Bi}_7\text{O}_9\text{I}_3$ (inset of **Fig. 3(a)**) and $\text{Bi}_4\text{O}_5\text{Br}_2$ (inset of **Fig. 3(b)**) revealed interplanar lattice spacings of 0.188 and 0.282 nm, respectively, corresponding to the (212) and (402) planes. For $\text{B-I}_{0.3}\text{Br}_{0.7}$ (inset of **Fig. 3(c)**), lattice fringes with a spacing of 0.285 nm were observed, which were slightly larger than those of the $\text{Bi}_4\text{O}_5\text{Br}_2$ lattice fringes (0.282 nm). Therefore, this interplanar spacing was indexed to the (402) plane of the $\text{B-I}_{0.3}\text{Br}_{0.7}$ crystalline structure [12,17], which is in agreement with the XRD results (**Fig. 1**). Moreover, the HRTEM images indicate good crystallinity of the $\text{Bi}_7\text{O}_9\text{I}_3$, $\text{Bi}_4\text{O}_5\text{Br}_2$, and $\text{B-I}_{0.3}\text{Br}_{0.7}$ particles. The scanning TEM image (**Fig. 3(d)**) and the corresponding scanning TEM–EDS elemental mappings of $\text{B-I}_{0.3}\text{Br}_{0.7}$ (**Fig. 3(e)–(h)**) clearly show a uniform distribution of the elements Bi, Br, I, and O throughout the $\text{B-I}_{0.3}\text{Br}_{0.7}$ micro-rod. Noticeably, the iodine signal was lower than the bromine signal, suggesting a lower iodine content in the $\text{B-I}_{0.3}\text{Br}_{0.7}$ solid solution, which is consistent with the detailed chemical composition reported in the EDS analysis.

The elemental compositions of $\text{Bi}_7\text{O}_9\text{I}_3$ and $\text{Bi}_4\text{O}_5\text{Br}_2$ determined via SEM-EDS revealed that the atomic ratios of Bi:I and Bi:Br in $\text{Bi}_7\text{O}_9\text{I}_3$ (**Fig. S1(a)**) and $\text{Bi}_4\text{O}_5\text{Br}_2$ (**Fig. S1(f)**) were 2.33 and 2.03, respectively, which is consistent with their stoichiometric ratios. The EDS spectra of the $\text{B-I}_x\text{Br}_{1-x}$ solid solutions (**Fig. S1(b)–(e)**) show the characteristic signals of Bi, O, Br, and I, indicating their co-existence in the $\text{B-I}_x\text{Br}_{1-x}$ solid solutions. Although the atomic ratios of I:Br in the $\text{B-I}_x\text{Br}_{1-x}$ solid solutions calculated from the EDS data were different from the expected elemental composition values, the atomic ratios of I:Br decreased, corresponding to a decrease in

the molar ratio of I:Br that was added to the precursors. According to Kirkendall diffusion, the larger radius of the I^- ion compared to the Br^- ion results in a lower diffusion rate in the reaction with the BiO^+ ion to form the $B-I_xBr_{1-x}$ nuclei. Thus, the unexpectedly low I^- content in the $B-I_xBr_{1-x}$ solid solutions was attributed to the diffusion-limited action of I^- ions in the reaction system. The contents of I and Br in the $B-I_xBr_{1-x}$ solid solution were quantitatively analyzed by ICP-MS, and the results presented in **Table S1** further confirmed that the I:Br molar ratio tended to decrease with a decrease in the feeding I:Br molar ratio.

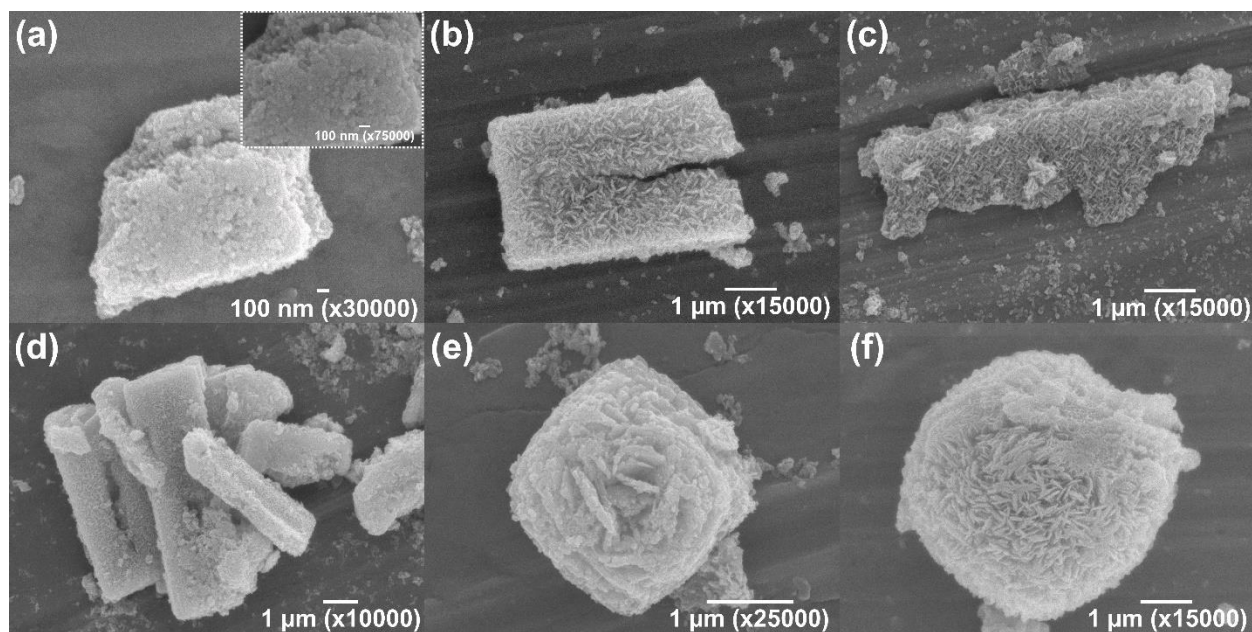


Fig. 2. SEM images of (a) $Bi_7O_9I_3$, (b) $B-I_{0.6}Br_{0.4}$, (c) $B-I_{0.4}Br_{0.6}$, (d) $B-I_{0.3}Br_{0.7}$, (e) $B-I_{0.2}Br_{0.8}$, and (f) $Bi_4O_5Br_2$. The inset of (a) shows the SEM image of $Bi_7O_9I_3$ at a higher magnification.

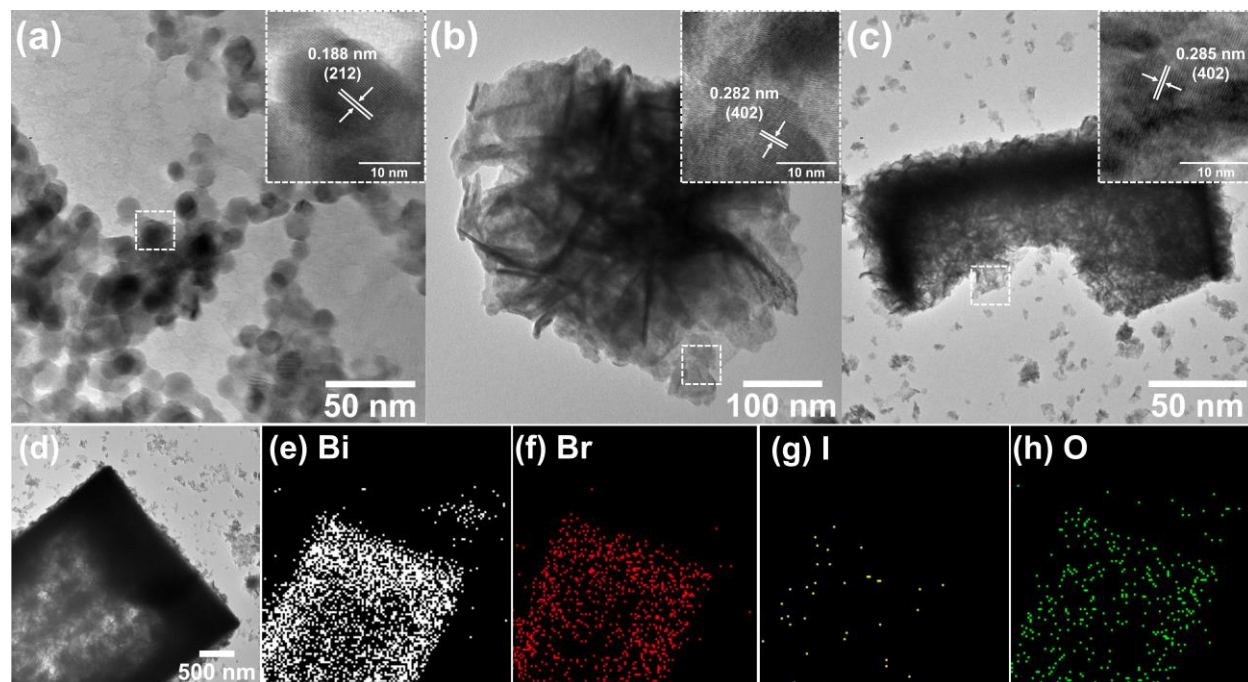


Fig. 3. TEM images of (a) $\text{Bi}_7\text{O}_9\text{I}_3$, (b) $\text{Bi}_4\text{O}_5\text{Br}_2$, and (c) $\text{B-I}_{0.3}\text{Br}_{0.7}$. The insets of (a)–(c) show the corresponding HRTEM images. (d) The STEM image and (e)–(h) the corresponding scanning TEM–EDS elemental mappings of $\text{B-I}_{0.3}\text{Br}_{0.7}$.

3.2. Chemical composition and state

The chemical composition and state at the sample surface were confirmed via XPS analysis, and the spectra are shown in **Fig. 4**. The full-length XPS spectra of $\text{Bi}_7\text{O}_9\text{I}_3$, $\text{Bi}_4\text{O}_5\text{Br}_2$, and $\text{B-I}_{0.3}\text{Br}_{0.7}$ (**Fig. 4(a)**) show their corresponding elements (Bi, O, Br, and I), confirming their high purity. The C 1s signal at 284.6 eV, which originates from adventitious carbon, was used for calibration against the relevant peaks. In **Fig. 4(b)**, two peaks were observed at 159.1–159.3 eV and 164.4–164.6 eV, corresponding to the Bi 4f_{7/2} and Bi 4f_{5/2} states, respectively, indicating the presence of Bi³⁺ in $\text{Bi}_7\text{O}_9\text{I}_3$, $\text{Bi}_4\text{O}_5\text{Br}_2$, and $\text{B-I}_{0.3}\text{Br}_{0.7}$ [12,46]. In the O 1s spectra (**Fig. 4(c)**), the broad bands can be deconvoluted into four peaks at binding energies of approximately 529, 531, 532, and 533 eV, suggesting four different states of O in the samples: Bi–O lattice oxygen [46,53],

hydroxyl groups adsorbed on the catalyst surface [46,53], oxygen species adsorbed at oxygen defects [54,55], and adsorbed water molecules [56], respectively. The I 3*d* spectrum of Bi₇O₉I₃ (**Fig. 4(d)**) displayed doublet peaks at binding energies of 619.2 and 630.7 eV, which were assigned to the I 3*d*_{5/2} and I 3*d*_{3/2} states, respectively, of I⁻ in Bi₇O₉I₃ [46]. The B-I_{0.3}Br_{0.7} solid solution exhibited two I 3*d* peaks at similar binding energies, but their intensities were significantly lower than those of Bi₇O₉I₃, indicating a lower I content on the surface of the solid solution than that in Bi₇O₉I₃. As shown in **Fig. 4(e)**, two peaks at binding energies of approximately 68 and 69 eV were found in both the Bi₄O₅Br₂ and B-I_{0.3}Br_{0.7} samples, which were attributed to the Br 3*d*_{5/2} and Br 3*d*_{7/2} spin-orbitals, respectively, indicating the monovalent oxidation state of Br in both samples [12]. Notably, the intensity of the Br 3*d* peak of the solid solution was comparable to that of Bi₄O₅Br₂, suggesting that Br⁻ rather than I⁻ was the major halide component in the solid solution, which is consistent with the EDS results (**Fig. S1**).

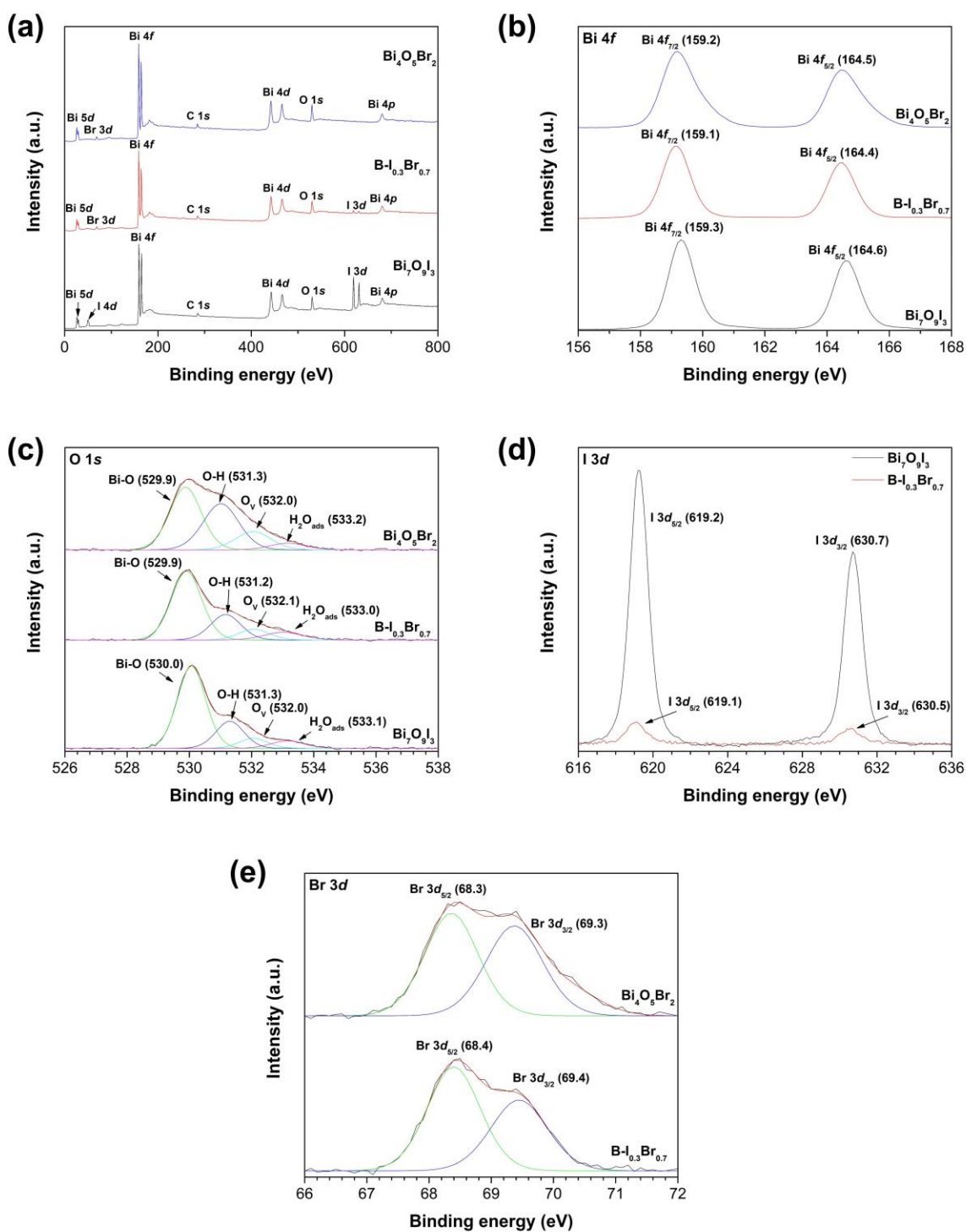


Fig. 4. XPS spectra of $\text{Bi}_7\text{O}_9\text{I}_3$, $\text{Bi}_4\text{O}_5\text{Br}_2$, and $\text{B-I}_{0.3}\text{Br}_{0.7}$ solid solutions: (a) survey, (b) Bi 4f, (c) O 1s, (d) I 3d, and (e) Br 3d.

3.3. Optical properties

The visible-light responsiveness of the synthesized samples was investigated via UV–Vis DRS, and the spectra are displayed in **Fig. 5**. The UV–Vis DRS spectra of the samples (**Fig. 5(a)**) show absorption edges in the visible-light region, suggesting that they can be employed as efficient photocatalytic materials under visible light. The absorption edges of $\text{Bi}_7\text{O}_9\text{I}_3$ and $\text{Bi}_4\text{O}_5\text{Br}_2$ were at 623.4 and 483.5 nm, respectively, and by employing the Tauc equation [37], the corresponding energy bandgaps were calculated to be 2.23 and 2.63 eV, respectively (**Fig. 5(b)**). With increasing I:Br molar ratio, the absorption edges of the $\text{B-I}_x\text{Br}_{1-x}$ solid solutions gradually shifted to wavelengths longer than those of $\text{Bi}_4\text{O}_5\text{Br}_2$. In addition, the Tauc plots of the $\text{B-I}_x\text{Br}_{1-x}$ solid solutions revealed narrower energy bandgaps than those of $\text{Bi}_4\text{O}_5\text{Br}_2$ (2.58, 2.56, 2.55, and 2.51 eV) for the $\text{B-I}_x\text{Br}_{1-x}$ solid solution with $x = 0.2, 0.3, 0.4, \text{ or } 0.6$, respectively). These results indicate that the formation of a solid solution is crucial for enhanced visible-light absorption ability, promoting the photogeneration of electrons and holes in solid-solution photocatalysts and consequently enhancing their photocatalytic properties.

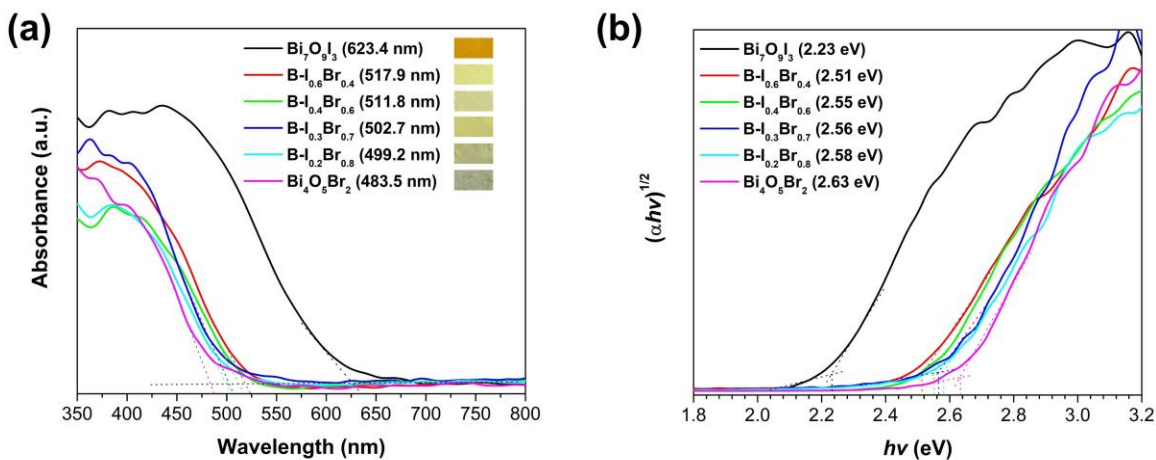


Fig. 5. (a) UV–Vis DRS spectra and (b) Tauc plots of the $\text{Bi}_7\text{O}_9\text{I}_3$, $\text{Bi}_4\text{O}_5\text{Br}_2$, and $\text{B-I}_x\text{Br}_{1-x}$ samples. The inset of (a) shows photographs of samples with various molar ratios of I:Br.

3.4. Electrochemical analysis

Transient photocurrent response, LSV and EIS measurements were conducted to evaluate the capability of the electrodes to generate and migrate charge carriers on the electrode surface. As seen from **Fig. 6(a)**, the photocurrent densities in ascending order were $\text{B-I}_{0.3}\text{Br}_{0.7}$, $\text{B-I}_{0.4}\text{Br}_{0.6}$, $\text{B-I}_{0.2}\text{Br}_{0.8}$, $\text{Bi}_4\text{O}_5\text{Br}_2$, $\text{B-I}_{0.6}\text{Br}_{0.4}$, and $\text{Bi}_7\text{O}_9\text{I}_3$, with estimated photocurrent densities of 0.51, 0.38, 0.30, 0.21, 0.13, and $0.08 \mu\text{A cm}^{-2}$, respectively. These results imply that the $\text{B-I}_{0.3}\text{Br}_{0.7}$ electrode generated and migrated more photogenerated charge carriers than the other electrodes [17]. Moreover, the LSV curves (**Fig. 6(b)**) revealed that the $\text{B-I}_{0.3}\text{Br}_{0.7}$ electrode exhibited the highest photocurrent density in the applied potential range, indicating the highest capability to produce photogenerated charge carriers [57]. This electrode also exhibited a negative shift in the onset potential, indicating that it was more suitable for the water oxidation process than other electrodes [58–60]. The Nyquist arc radii of the EIS plots were recorded to evaluate the charge-separation and migration efficiencies of the electrodes. As shown in **Fig. 6(c)**, the $\text{B-I}_{0.3}\text{Br}_{0.7}$ electrode exhibited the smallest Nyquist arc radius, indicating the lowest charge-transfer resistance on the electrode surface [17]. Thus, the superior photocatalytic activity of $\text{B-I}_{0.3}\text{Br}_{0.7}$ can be attributed to more efficient separation and migration of photogenerated charge carriers under visible-light irradiation.

To determine the conduction- and valence-band potentials of the $\text{B-I}_x\text{Br}_{1-x}$ solid solutions in comparison to those of $\text{Bi}_7\text{O}_9\text{I}_3$ and $\text{Bi}_4\text{O}_5\text{Br}_2$, Mott–Schottky plots were recorded. As shown in **Fig. 6(d)** and **Fig. S2**, all samples exhibited the characteristics of n-type semiconductors, as

indicated by the positive slopes of the Mott–Schottky plots [53]. By extrapolating the tangents to the potential axis ($1/C^2 = 0$), the flat-band potentials (E_{FB}) of $\text{Bi}_7\text{O}_9\text{I}_3$, $\text{B-I}_{0.3}\text{Br}_{0.7}$, and $\text{Bi}_4\text{O}_5\text{Br}_2$ were determined to be 0.18, -0.022 , and -0.050 V (*vs.* NHE), respectively. Similarly, the E_{FB} of $\text{B-I}_{0.6}\text{Br}_{0.4}$, $\text{B-I}_{0.4}\text{Br}_{0.6}$, and $\text{B-I}_{0.2}\text{Br}_{0.8}$ were 0.028, -0.013 , and -0.024 V (*vs.* NHE), respectively (**Fig. S2**). The conduction-band potential (E_{CB}) of an n-type semiconductor is approximately 0.1 eV higher than its E_{FB} value. Hence, the E_{CB} values for $\text{Bi}_7\text{O}_9\text{I}_3$, $\text{B-I}_{0.6}\text{Br}_{0.4}$, $\text{B-I}_{0.4}\text{Br}_{0.6}$, $\text{B-I}_{0.3}\text{Br}_{0.7}$, $\text{B-I}_{0.2}\text{Br}_{0.8}$, and $\text{Bi}_4\text{O}_5\text{Br}_2$ were estimated to be 0.08, -0.07 , -0.11 , -0.12 , -0.12 , and -0.15 V (*vs.* NHE), respectively. Based on the calculated energy bandgap values (**Fig. 5(b)**), the respective valence-band potentials (E_{VB}) of these semiconductors were calculated to be 2.31, 2.44, 2.44, 2.44, 2.46, and 2.48 V (*vs.* NHE), respectively. A schematic of the band potentials of the semiconductors (**Fig. 6(e)**) shows that the band potentials of the solid solutions could be tuned according to their I:Br molar ratios. The valence-band potentials of the $\text{B-I}_x\text{Br}_{1-x}$ solid solutions were more positive than that of $\text{Bi}_7\text{O}_9\text{I}_3$, facilitating photooxidation via the reactive species. In addition, the more negative conduction-band potentials of the $\text{B-I}_x\text{Br}_{1-x}$ solid solutions compared to those of $\text{Bi}_7\text{O}_9\text{I}_3$ were essential for simultaneously producing electrons with stronger reductive abilities.

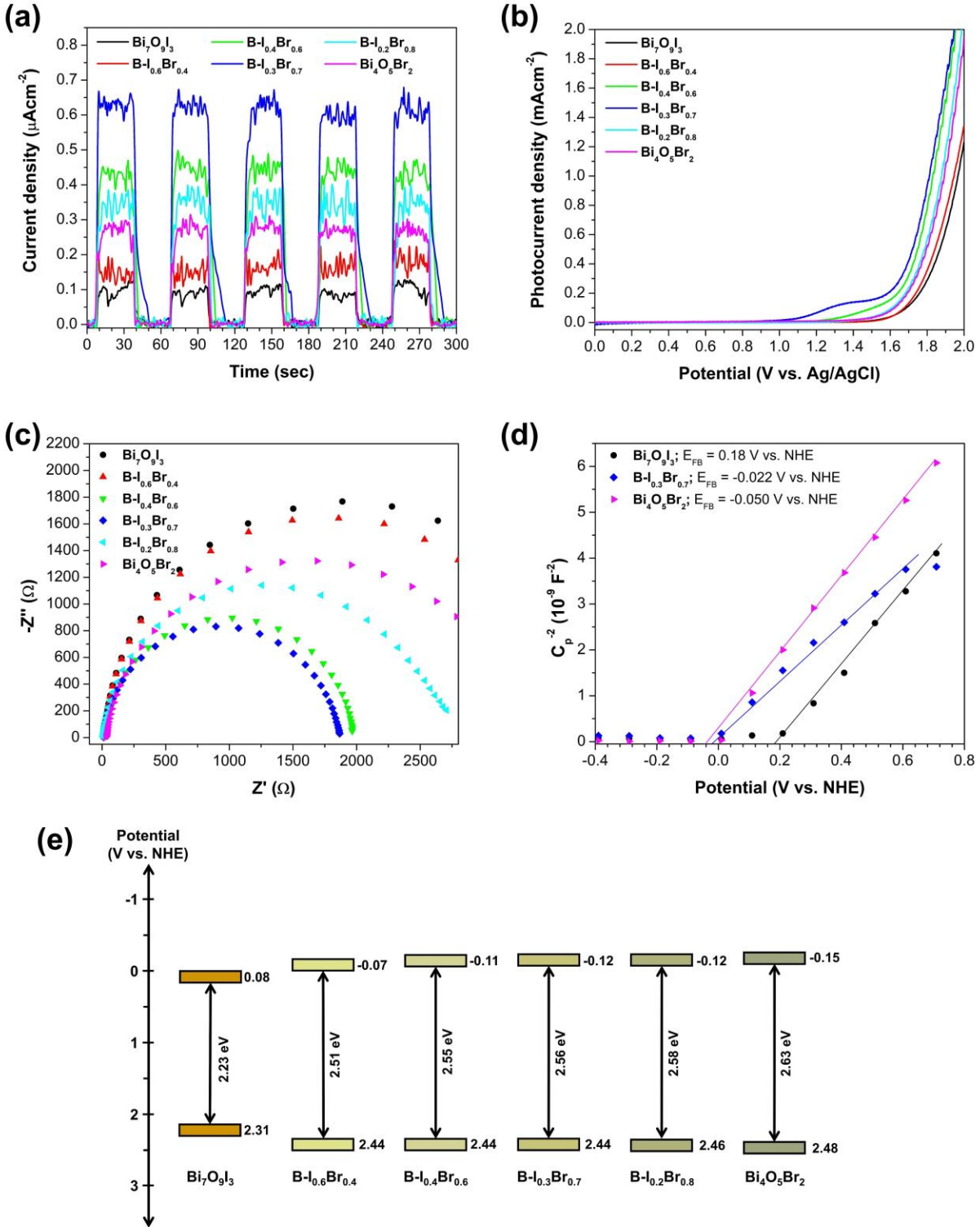


Fig. 6. (a) Transient photocurrent responses, (b) LSV curves, (c) EIS plots, (d) Mott-Schottky plots, and (e) band potentials of $\text{Bi}_7\text{O}_9\text{I}_3$, $\text{Bi}_4\text{O}_5\text{Br}_2$, and $\text{B-I}_x\text{Br}_{1-x}$ solid solutions.

3.5. Photodegradation of phenolic compounds

The photocatalytic properties of the prepared samples were evaluated via the photodegradation of 4NP under visible-light irradiation, with the results presented in **Fig. 7**. As shown in **Fig. 7(a)**, the %DE values of $\text{Bi}_7\text{O}_9\text{I}_3$ and $\text{Bi}_4\text{O}_5\text{Br}_2$ are 8.4% and 53.6%, respectively. Compared with $\text{Bi}_7\text{O}_9\text{I}_3$, the $\text{B-I}_x\text{Br}_{1-x}$ solid solutions showed greater photocatalytic activity for 4NP degradation. After 360 min of irradiation, the %DEs values were 82.2, 98.7, 87.9, and 17.4% for $\text{B-I}_{0.2}\text{Br}_{0.8}$, $\text{B-I}_{0.3}\text{Br}_{0.7}$, $\text{B-I}_{0.4}\text{Br}_{0.6}$, and $\text{B-I}_{0.6}\text{Br}_{0.4}$, respectively. According to the kinetic plots (**Fig. 7(b)**), the $\text{B-I}_{0.3}\text{Br}_{0.7}$ solid solution exhibited the highest rate constant (k_{app}) of 0.0064 min^{-1} , which was, respectively, 32 and 4 times higher than those of $\text{Bi}_7\text{O}_9\text{I}_3$ (0.0002 min^{-1}) and $\text{Bi}_4\text{O}_5\text{Br}_2$ (0.0016 min^{-1}). Therefore, the $\text{B-I}_{0.3}\text{Br}_{0.7}$ solid solution was considered the optimal photocatalyst, with the highest photodegradation efficiency and rate for 4NP. It should be noted that, even though the BET surface area of the $\text{B-I}_{0.3}\text{Br}_{0.7}$ solid solution ($21.8 \text{ m}^2\text{g}^{-1}$) was lower than that of $\text{Bi}_7\text{O}_9\text{I}_3$ ($24.3 \text{ m}^2\text{g}^{-1}$) and $\text{Bi}_4\text{O}_5\text{Br}_2$ ($47.0 \text{ m}^2\text{g}^{-1}$), the solid solution exhibited greatly enhanced photocatalytic activity. This implies that the surface area of these materials did not significantly influence their photocatalytic activity.

In light of the superiority of the $\text{B-I}_{0.3}\text{Br}_{0.7}$ solid solution for 4NP degradation, its universality in degrading other phenolic compounds (3NP and BPA) was evaluated under identical photocatalytic conditions. As shown in **Fig. 7(c)**, the percentage of DEs after 180 min of light exposure followed the order BPA (97.5%) > 4NP (72.8%) > 3NP (27.5%), which corresponds well with the k_{app} values in **Fig. 7(d)**. In contrast, the ability of the $\text{B-I}_{0.3}\text{Br}_{0.7}$ solid solution to adsorb these phenolic compounds in the dark was less than 1%. Moreover, the concentration of these phenolic compounds did not change significantly during irradiation, indicating their negligible

photolysis under visible light. These findings confirm the degradation of phenolic compounds via photocatalysis. The k_{app} values of the B-I_{0.3}Br_{0.7} solid-solution photocatalyst in this work, compared with the previous literature reports, are shown in **Table S2**. The different in the degradation rates presented in **Table S2** could be caused by variations in the photocatalytic conditions, such as the type and power of the light source, photocatalyst dosage, and concentration of the target pollutants. In addition, the characteristics of the photocatalysts likely affected the degradation rate. Photocatalytic data with error bars based on the standard deviations of the three parallel experiments are presented in **Fig. S3**. The small standard deviation for each irradiated time interval reflects the accuracy of the sample data.

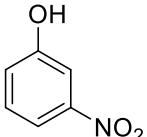
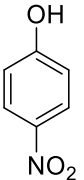
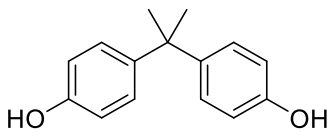
The difference in the photodegradation efficiencies of the phenolic compounds could be attributed to their different chemical structures (**Table 1**). Substituents on benzene derivatives can be classified into two groups [61]: electron-donating (e.g., the hydroxyl group (–OH)) and electron-withdrawing (e.g., the nitro group (–NO₂)), which influence the electrophilic attack of the benzene ring on the reactive species during photocatalysis (e.g., the electrophilic hydroxyl radical (•OH) and/or hole (h⁺)). The substituent groups on the benzene derivatives significantly affect the electron density of the benzene ring and the rate of electrophilic substitution of the hydrogen atom and nitro group on the benzene ring by the •OH radical at the initial stage of the photodegradation reaction [62]. In principle, the electron-donating substituent (–OH) increases the electron density on the carbons in *ortho*- and *para*- positions of the benzene ring compared to the *meta*- position, facilitating electrophilic attack at the *ortho*- and *para*- positions. In contrast, the electron-withdrawing substituent (–NO₂) deactivates the aromatic structure toward electrophilic attack by reducing the electron density on the carbons in *ortho*- and *para*- positions of the benzene ring.

In 3-nitrophenol (3NP), one of the hydrogens “*meta*” to the –OH group is replaced by a nitro (–NO₂) group, which deactivates the *ortho*- and *para*- positions for electrophilic substitution. Therefore, 3-nitrophenol is much less susceptible to photodegradation than other phenolic compounds [62]. In the case of 4-nitrophenol (4NP), one of the hydrogens “*para*” to the –OH group is replaced by a –NO₂ group, which increases the electron density on the carbons “*ortho*” and “*para*” to the –OH group, as compared to those in the *meta*- position. Meanwhile, the electron densities on the carbons “*ortho*” to the –NO₂ group and “*meta*” to the –OH group, decrease. Consequently, the –OH group still activates the benzene ring, and electrophilic attack preferentially occurs at the *ortho*- and/or *para*- positions with respect to the –OH group. Therefore, the photodegradation efficiency of 4NP is higher than that of 3NP [2,3,63–65]. Moreover, the presence of the –NO₂ group at the *para*- position of 4NP resulted in effective resonance structures of its conjugated base, facilitating electrophilic attack by •OH and/or h⁺. Unlike 4NP, 3NP cannot delocalize the charge owing to the presence of the –NO₂ group in the *meta*- position, resulting in a low degradation rate of 3NP against electrophilic attack [2,3,64]. Finally, the higher photodegradation efficiency of BPA compared to 4NP and 3NP could be attributed to its symmetrical molecular structure, which can directly undergo aromatic ring-opening reactions during photocatalytic degradation and, consequently, can easily decompose, resulting in a higher photodegradation efficiency. In contrast, the photocatalysis of 4NP and 3NP requires multistep reactions before decomposition is complete [66–68].

Because actual wastewater is usually contaminated with several phenolic compounds, the photocatalytic degradation of 4NP and BPA in a coexisting 4NP–BPA system under visible-light irradiation was also investigated. The photodegradation of 4NP and BPA in the coexisting 4NP–BPA system over the B-I_{0.3}Br_{0.7} solid-solution photocatalyst was performed by varying the

4NP concentration at 5 and 10 ppm and fixing the BPA concentration at 10 ppm. Without the addition of the B-I_{0.3}Br_{0.7} photocatalyst, the UV–Vis absorption spectra of 4NP and BPA in the coexisting 4NP–BPA system shown in **Fig. S4(a)** reveal that the spectra of the 4NP and BPA partially overlap. Therefore, it was difficult to measure the maximum absorption wavelength (λ_{\max}) of BPA. However, the photodegradation of 4NP and BPA can be roughly investigated by considering changes in their absorption intensities. **Fig. S4(b) and (c)** show the changes in the UV–Vis absorption spectra of 4NP and BPA in the coexisting 4NP–BPA systems over the B-I_{0.3}Br_{0.7} photocatalyst after visible-light irradiation at different time intervals (0-360 min). It can be seen that the absorption intensity of the BPA spectra gradually decreased upon increasing irradiation time, whereas the absorption intensity of the 4NP spectra changed slightly even using either 5 or 10 ppm of 4NP. The retardation in the photodegradation efficiency of 4NP in the coexisting 4NP–BPA system could be due to the relatively high degradation rate of BPA compared to 4NP, as shown in **Fig. 7**. These findings suggest a competitive photodegradation between 4NP and BPA, highlighting the high potential of this photocatalyst for the selective photodegradation of BPA.

Table 1. Chemical structures of the phenolic compounds.

Phenolic compounds		
<i>3-nitrophenol</i>	<i>4-nitrophenol</i>	<i>bisphenol A</i>
		

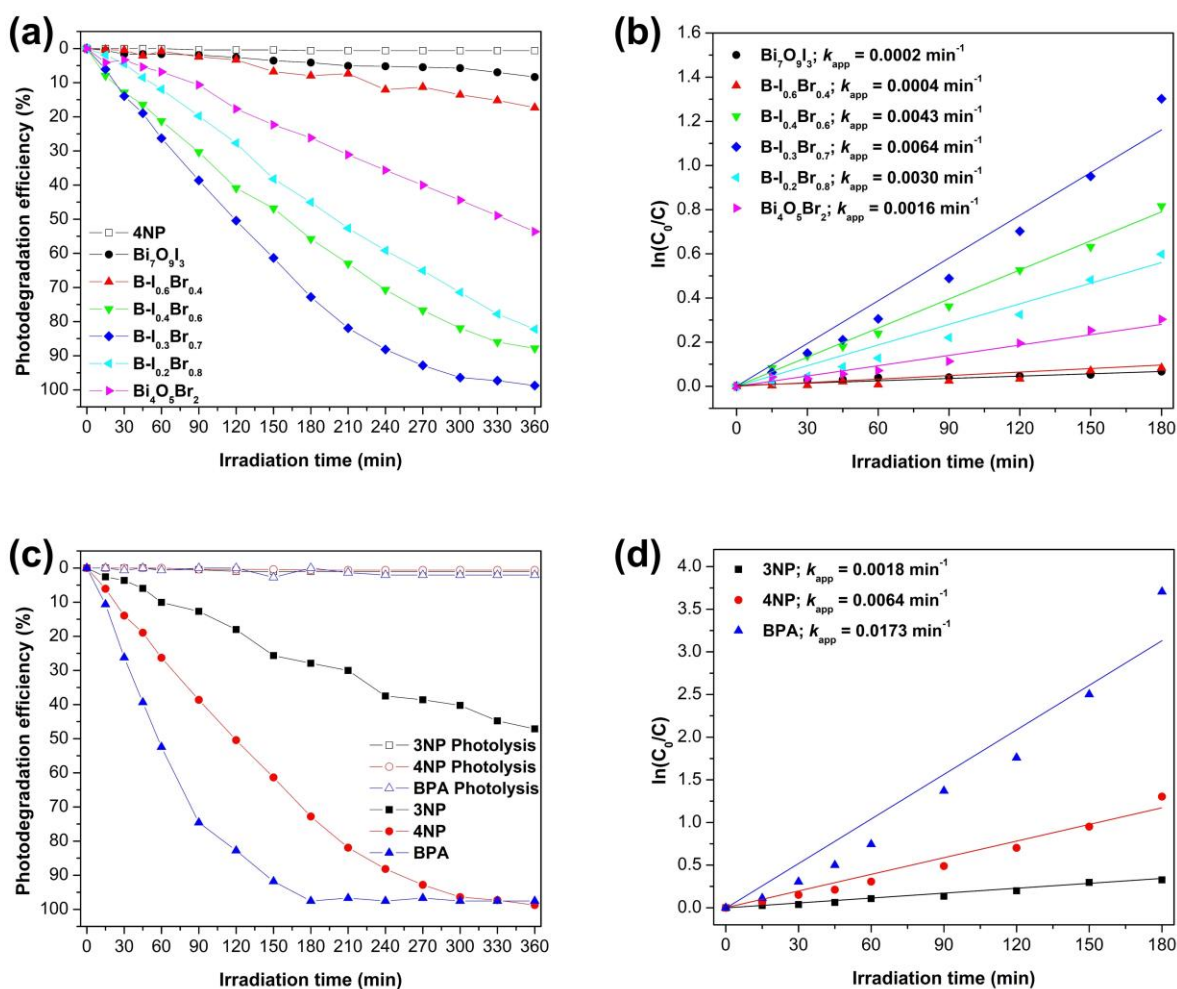


Fig. 7. (a) Photodegradation efficiencies and (b) kinetic plots of 4NP over $\text{Bi}_7\text{O}_9\text{I}_3$, $\text{Bi}_4\text{O}_5\text{Br}_2$, and $\text{Bi-I}_x\text{Br}_{1-x}$ solid solutions under visible-light irradiation. (c) Photodegradation efficiencies and (d) kinetic plots of 3NP, 4NP, and BPA over $\text{Bi-I}_{0.3}\text{Br}_{0.7}$ solid solution.

3.6. Mechanistic insights

A series of reactive-species trapping experiments was performed by adding BQ, EDTA-2Na, and IPA (scavengers for $\cdot\text{O}_2^-$, h^+ , and $\cdot\text{OH}$, respectively) to the 4NP solution under identical reaction conditions. The addition of these scavengers markedly decreased the photodegradation efficiency, indicating that the $\cdot\text{O}_2^-$, h^+ , and $\cdot\text{OH}$ reactive species participated in photocatalytic

degradation (**Fig. 8(a)**). However, the h^+ on the surface of the Bi-based photocatalyst could not directly oxidize OH^- or H_2O to the $\bullet OH$ radical owing to the higher negative reduction potential of Bi^{5+}/Bi^{3+} (1.59 eV) than the standard reduction potentials of $\bullet OH/H_2O$ (2.27 eV) and $\bullet OH/OH^-$ (1.99 eV) [50,69,70]. Under visible-light irradiation, the excited electrons in the CB react with dissolved O_2 in the reaction solution to produce $\bullet O_2^-$, which subsequently produces H_2O_2 via a multielectron oxygen-reduction process and then generates $\bullet OH$ [71–73]. Therefore, the $\bullet OH$ radical was indirectly generated by activating molecular oxygen, whereas the h^+ in the VB of the solid solution directly reacted with the 4NP molecules.

The generation of H_2O_2 and $\bullet OH$ was detected via *o*-tolidine oxidation [43,44] and TA-PL probing methods [45], respectively, under visible-light irradiation. As shown in **Fig. 8(b)**, the absorbance of the oxidized *o*-tolidine in the $Bi_7O_9I_3$, $Bi_4O_5Br_2$, and $B-I_{0.3}Br_{0.7}$ photocatalytic systems at 446 nm steadily increased upon light irradiation, suggesting that H_2O_2 was detectable in the system [43,74,75]. Additionally, the $B-I_{0.3}Br_{0.7}$ solid solution exhibited higher H_2O_2 generation efficiency than $Bi_7O_9I_3$ and $Bi_4O_5Br_2$, indicating superior charge separation and migration efficiencies. **Fig. S5** shows the fluorescence emission spectra of the 2-hydroxyterephthalic acid (TAOH) solution, the fluorescent product of the reaction between $\bullet OH$ and terephthalic acid (TA), over the $B-I_{0.3}Br_{0.7}$ photocatalyst under visible-light irradiation. The increase in the fluorescence intensity of TAOH, along with a longer visible-light irradiation time, indicates the generation of $\bullet OH$ in the photocatalyst system.

The NBT method was employed to further examine the production of $\bullet O_2^-$ radicals on the $B-I_{0.3}Br_{0.7}$ surface. After 360 min of visible-light irradiation, the percentage of NBT transformed over the $B-I_{0.3}Br_{0.7}$ solid solution was 25.1% (**Fig. 8(c)**), which was considerably higher than the percentage transformed over both $Bi_7O_9I_3$ (0.7%) and $Bi_4O_5Br_2$ (13.4%). This indicates a higher

efficiency for the generation of reactive $\bullet\text{O}_2^-$ radicals, which could be attributed to the improved charge separation and migration in the $\text{B-I}_{0.3}\text{Br}_{0.7}$ solid solution. In addition, the aforementioned analyses indicate that the $\text{B-I}_{0.3}\text{Br}_{0.7}$ solid-solution photocatalyst activated molecular oxygen to produce $\bullet\text{O}_2^-$, which subsequently produced other reactive species, including H_2O_2 and $\bullet\text{OH}$ [15], promoting its photocatalytic activity.

A photocatalytic mechanism for 4NP degradation over the $\text{B-I}_{0.3}\text{Br}_{0.7}$ solid-solution photocatalyst was then proposed (**Fig. 8(d)**). Upon visible-light irradiation, electrons in the VB of the photocatalyst are excited to the CB, leaving behind holes in the VB. Owing to the more negative E_{CB} of $\text{B-I}_{0.3}\text{Br}_{0.7}$ (-0.12 V vs. NHE) than the standard reduction potential of $\text{O}_2/\bullet\text{O}_2^-$ (-0.046 V vs. NHE) [76], the strongly reductive excited electrons in the CB reduced the dissolved oxygen molecules to $\bullet\text{O}_2^-$ radicals. As evidenced by the trapping experiments, the TA-PL probing method, and the o-tolidine oxidation, the $\bullet\text{O}_2^-$ radicals were further reduced via a multielectron oxygen-reduction process to form H_2O_2 molecules. The short-lived H_2O_2 molecules eventually dissociated into $\bullet\text{OH}$ radicals, which were responsible for the photodegradation of 4NP. Meanwhile, the photogenerated holes in the VB of $\text{B-I}_{0.3}\text{Br}_{0.7}$ directly participated in photocatalytic degradation [53].

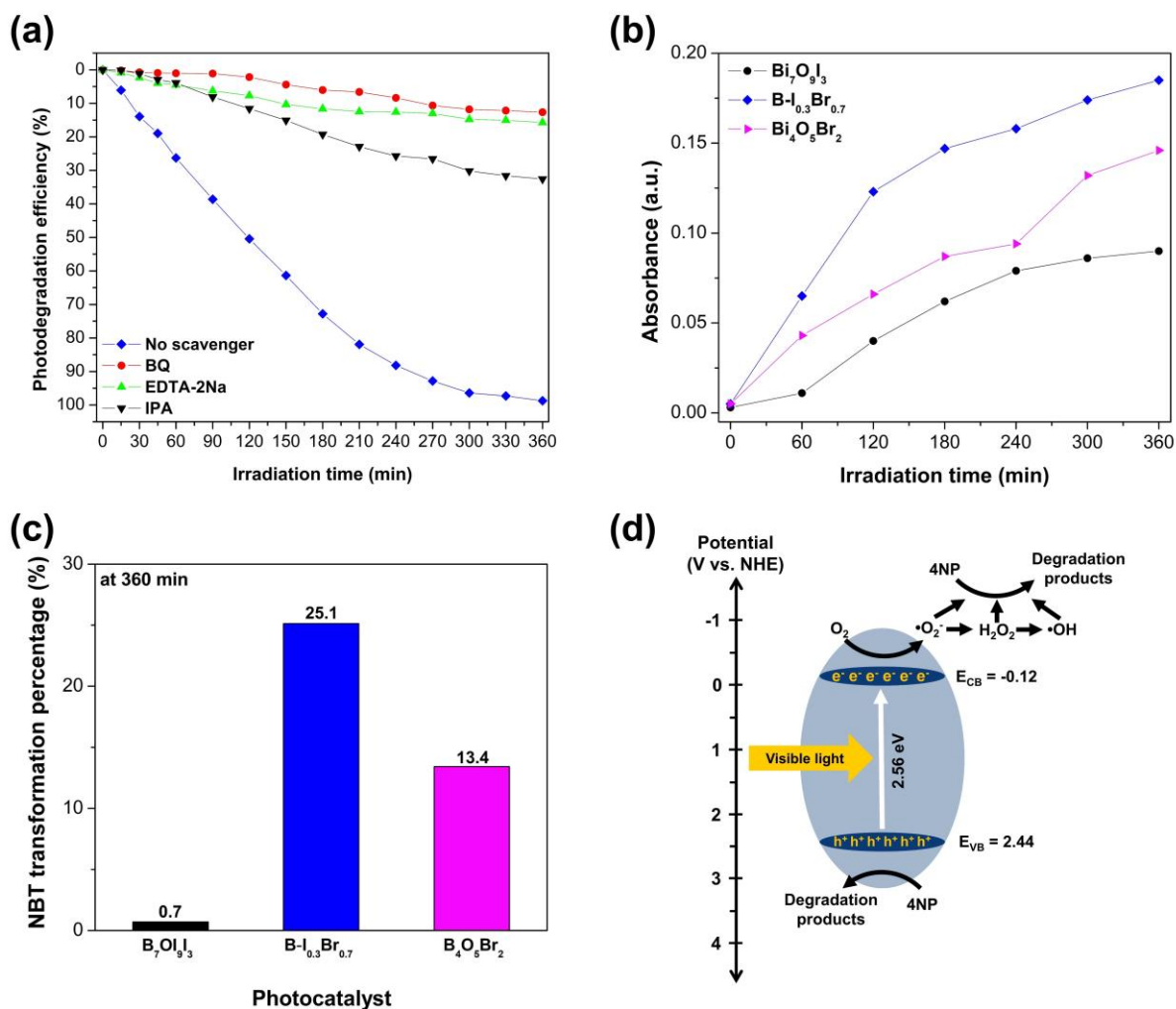


Fig. 8. (a) Effect of various scavengers on the photocatalytic degradation of 4NP, (b) time-dependent absorbance at 446 nm of the 2-electron oxidized *o*-tolidine, (c) NBT transformation percentages over Bi₇O₉I₃, Bi₄O₅Br₂, and B-I_{0.3}Br_{0.7} after 360 min of visible-light irradiation, and (d) a proposed mechanism for the photocatalytic degradation of 4NP over the B-I_{0.3}Br_{0.7} solid solution.

3.7. RhB-sensitization effect on 4NP and BPA photodegradation

As previously reported [37,77,78], RhB is an effective photosensitizer and promotes the photocatalytic activity of bismuth oxyhalide photocatalysts by injecting photoexcited electrons

into the CB. In this study, the photodegradation of pollution systems containing selected phenolic compounds (4NP and BPA) combined with rhodamine B (RhB), a representative of organic dye, were further investigated. The simultaneous photodegradation of 4NP and RhB in the 4NP–RhB combined pollution system over the $\text{B-I}_{0.3}\text{Br}_{0.7}$ solid-solution photocatalyst was performed by fixing the 4NP concentration at 10 ppm and varying the RhB concentration between 5 and 10 ppm. In the 4NP–RhB combined pollution system, enhanced photocatalytic degradation of 4NP, one of the main target pollutants, was expected; however, the %DE of 4NP was reduced significantly, from 98.7% to 25.7%, after the addition of 5 ppm of RhB (**Fig. 9(a)**), whereas more than 80% of the RhB was degraded within 30 min of light irradiation (**Fig. 9(b)**). The significant decrease in the photodegradation efficiency of 4NP in the 4NP–RhB combined pollution system was attributed to the rapid degradation of the RhB molecules via the consumption of photogenerated holes [41]. To verify this, we doubled the concentration of RhB (10 ppm), and the photodegradation of 4NP during the first hour of irradiation was found to be slightly higher. It stabilized at 23.4% after prolonged irradiation, which was still lower than that in the 4NP single-pollution system (98.7% at 360 min). However, under these conditions, RhB degraded rapidly and it had been completely degraded within 270 min of light irradiation. These results suggest that the photodegradation of 4NP cannot be improved via RhB sensitization owing to the competition in photodegradation between RhB and 4NP.

Subsequently, we carried out the simultaneous photodegradation of BPA and RhB in the BPA–RhB combined pollution system to investigate the sensitization effect of RhB on BPA photodegradation. The presence of either 5 or 10 ppm RhB in the BPA solution (10 ppm) significantly improved the photodegradation efficiency of BPA, from 26.2% to approximately 92%, in 60 min (**Fig. 9(c)**). Over the same irradiation time, 70–80% of RhB was simultaneously

degraded (**Fig. 9(d)**). This suggests that the significantly enhanced photodegradation efficiency of BPA could be attributed to the RhB-sensitization process, because the photodegradation efficiencies of BPA and RhB were comparable. Furthermore, the sensitization process was preserved because of the gradual photodegradation of RhB with BPA. In the BPA–RhB (10 ppm) combined solution system, RhB photodegradation decreased during the initial period of light irradiation, whereas BPA photodegradation did not change significantly. Therefore, the introduction of only 5 ppm of RhB into the BPA–RhB combined pollution system was deemed sufficient for improving BPA photodegradation.

To examine the effect of the RhB-sensitization mechanism in terms of molecular oxygen activation on the surface of the B-I_{0.3}Br_{0.7} photocatalyst, an RhB solution was added to a suspension of NBT and the B-I_{0.3}Br_{0.7} photocatalyst, and the time-dependent formation of •O₂⁻ was investigated [77]. RhB (5 ppm) significantly improved the percentage of NBT transformation (**Fig. 10(a)**). After 15 min of light irradiation, the NBT transformation percentage (17.9%) was 5.3 times that without RhB addition (3.4%), illustrating enhanced molecular oxygen activation due to the B-I_{0.3}Br_{0.7} solid solution. Moreover, the NBT transformation percentage steadily increased and reached 26.5% after 360 min of irradiation, which coincided with a progressive blue shift in the maximum absorption wavelength (λ_{\max}) of RhB (**Fig. 10(b)**), resulting from the rapid decomposition of RhB molecules to *N*-de-ethylated intermediates via *N*-de-ethylation [37,79]. The formation of *N*-de-ethylated intermediates inhibited the RhB-sensitization process; therefore, the number of •O₂⁻ radicals generated was unexpectedly low (NBT transformation percentage = 26.5%). Upon increasing the RhB concentration from 5 to 10 ppm, the NBT transformation percentage doubled to 51.1% (**Fig. 10(c)**), which is correlated with a higher generation of •O₂⁻

radicals. This indicates that the $B-I_{0.3}Br_{0.7}$ solid solution could be sensitized via RhB molecules rather than *N*-de-ethylated intermediates.

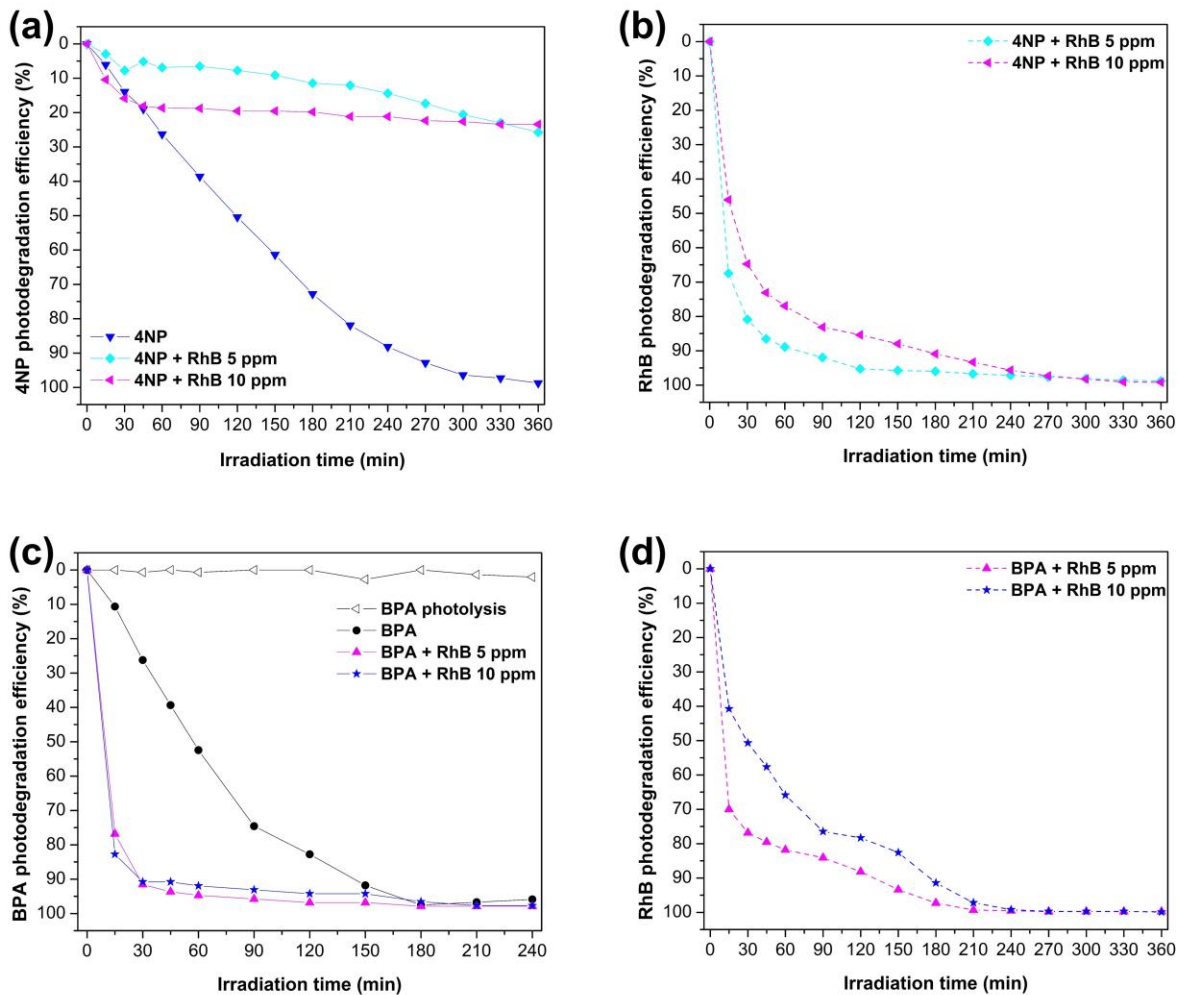


Fig. 9. Photodegradation efficiencies of (a) 4NP and (b) RhB in the 4NP–RhB combined system, and (c) BPA and (d) RhB in the BPA–RhB combined system over the $B-I_{0.3}Br_{0.7}$ solid-solution photocatalyst under visible-light irradiation.

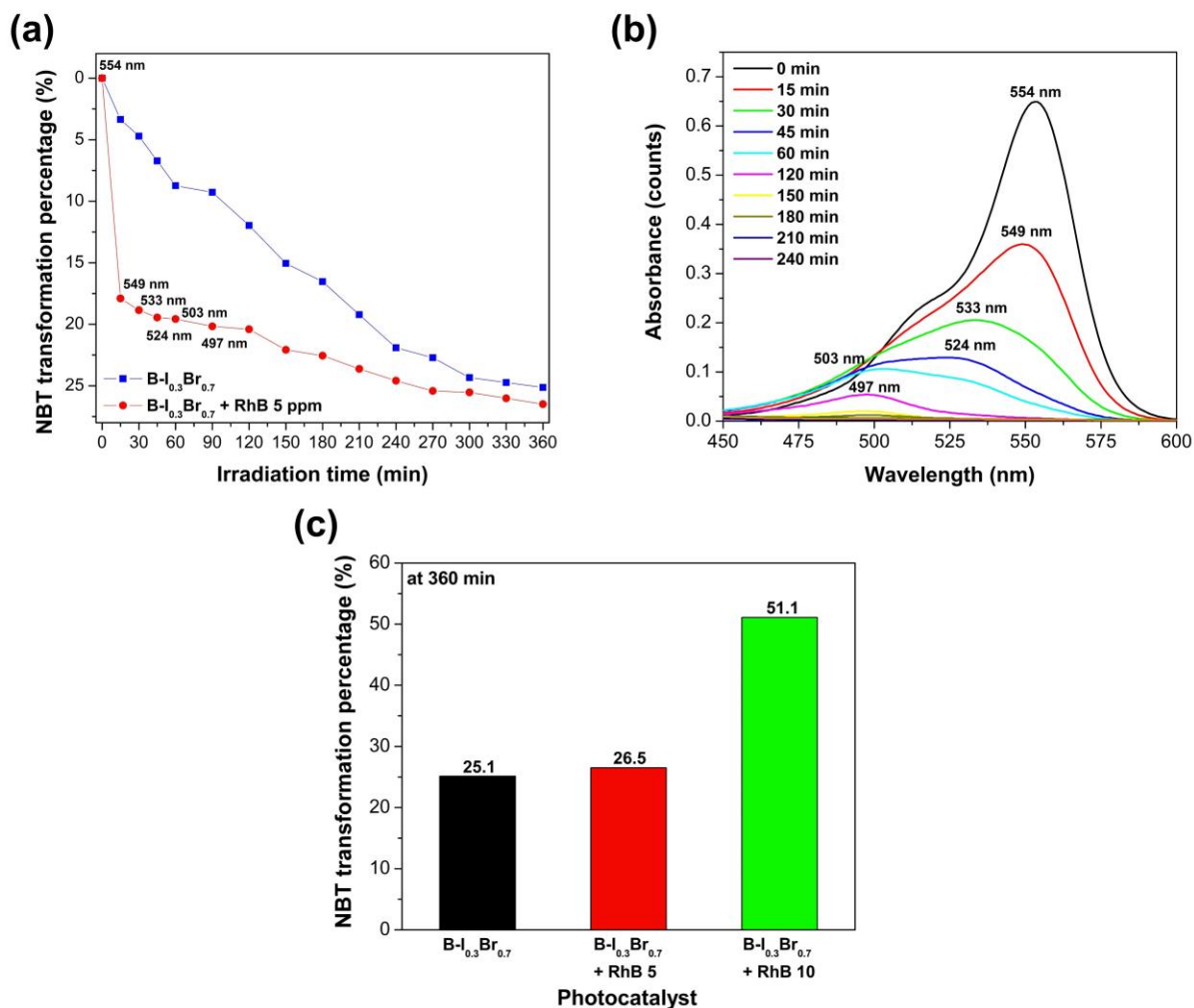


Fig. 10. (a) NBT transformation percentages over the B-I_{0.3}Br_{0.7} solid solution with and without RhB (5 ppm), (b) changes in the absorption spectra of RhB (5 ppm) during the NBT-transformation test over the B-I_{0.3}Br_{0.7} solid solution, and (c) NBT transformation percentages over the B-I_{0.3}Br_{0.7} solid solution with and without RhB (5 and 10 ppm) after 360 min of irradiation.

The reusability and stability of the B-I_{0.3}Br_{0.7} solid-solution photocatalyst are important for its practical application, and were tested by reusing it for the simultaneous photocatalytic degradation of BPA and RhB in a BPA–RhB combined system for four successive runs under

identical conditions. **Fig. 11(a)–(b)** show that the high photodegradation efficiency of $B-I_{0.3}Br_{0.7}$ for both BPA and RhB was maintained over four consecutive cycles, demonstrating its reusability. Additionally, there were no obvious changes in the crystallinity, phase, structure, and morphology of $B-I_{0.3}Br_{0.7}$ before and after the recycling experiments, as revealed by the XRD patterns (**Fig. 11(c)**) and SEM image (**Fig. 11(d)**) of the used $BOI_{0.3}Br_{0.7}$ photocatalyst, indicating excellent stability and durability during the photocatalytic process.

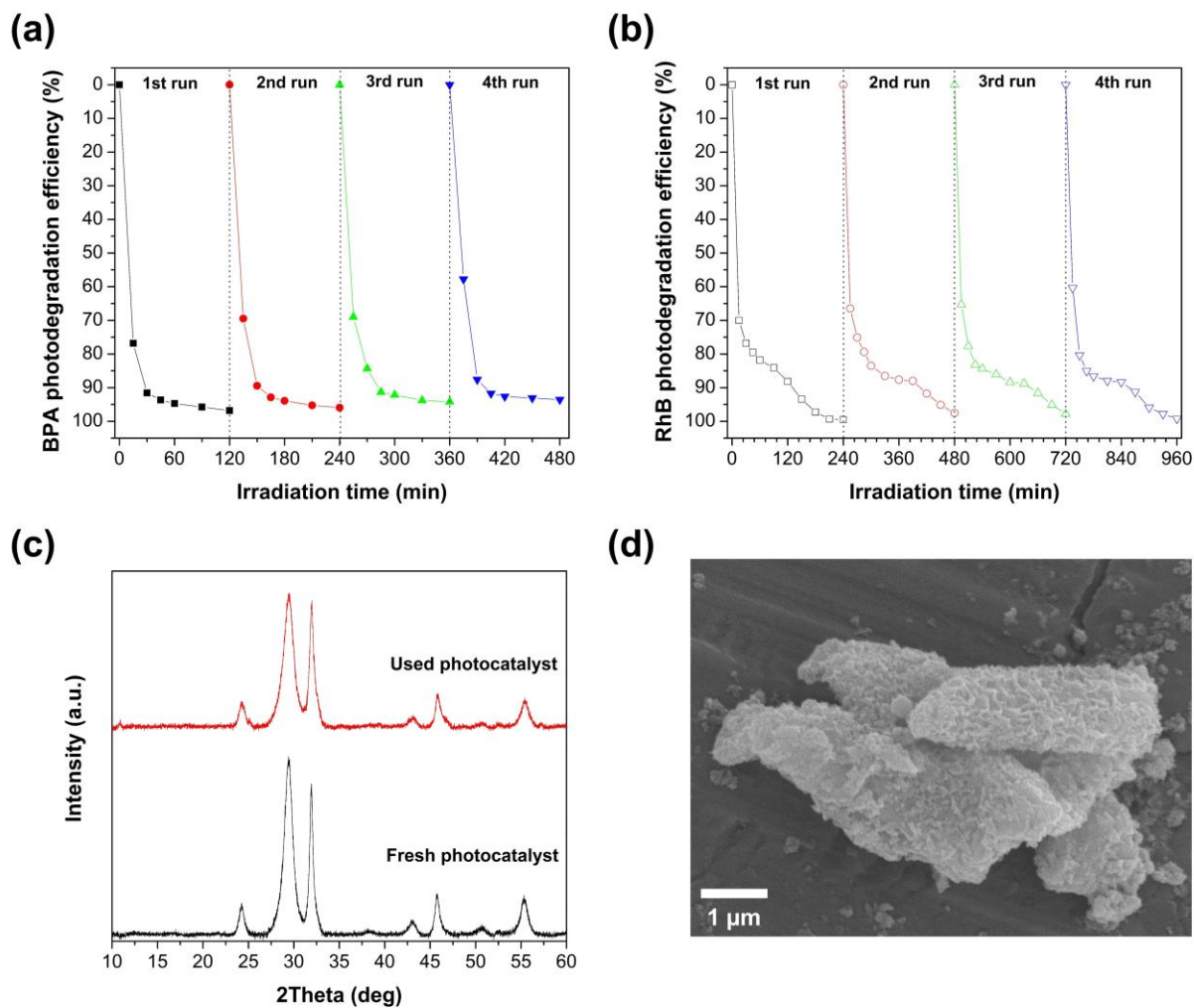


Fig. 11. Recycling experiments of the $B-I_{0.3}Br_{0.7}$ solid solution toward photocatalytic degradation of (a) BPA and (b) RhB in the BPA–RhB combined system. (c) XRD spectra of the $B-I_{0.3}Br_{0.7}$

solid solution before and after four cycles of photocatalytic reactions. (d) The corresponding SEM image of the used B-I_{0.3}Br_{0.7} photocatalyst.

4. Conclusion

Bi₇O₉I₃–Bi₄O₅Br₂ solid solutions (B-I_xBr_{1-x}, where $x = 0.2, 0.3, 0.4,$ or 0.6) were successfully synthesized via a facile and rapid microwave radiation method. The energy structures and bandgaps of the B-I_xBr_{1-x} solid solutions were tuned by varying the I:Br molar ratio. Combinations of Bi-rich and solid-solution strategies promoted visible-light induced charge generation, separation, and migration, thereby achieving enhanced photocatalytic activities. Compared with Bi₇O₉I₃ and Bi₄O₅Br₂, the Bi₇O₉I₃–Bi₄O₅Br₂ solid solution with an I:Br molar ratio of 0.3:0.7 (B-I_{0.3}Br_{0.7}) showed superior photocatalytic degradation of 4-nitrophenol under visible-light irradiation, owing to the enhanced generation, separation, and migration of charge carriers, as revealed by electrochemical analyses. Additionally, the B-I_{0.3}Br_{0.7} photocatalyst was used to degrade other phenolic compounds, including 3-nitrophenol and bisphenol A, and the difference in the photodegradation efficiencies of these compounds was associated with their chemical structures. Trapping experiments, *o*-tolidine oxidation, terephthalic acid photoluminescence, and nitroblue tetrazolium transformation methods confirmed the roles of •O₂⁻, •OH, and h⁺ in 4-nitrophenol photodegradation. Compared with Bi₇O₉I₃, the strong reducing ability of the excited electrons in the B-I_{0.3}Br_{0.7} solid solution facilitated the activation of molecular oxygen to generate •O₂⁻, H₂O₂, and •OH reactive species. Furthermore, in the coexisting system of bisphenol A and rhodamine B dye, the synergistic effect of rhodamine B dye exclusively promoted the degradation of bisphenol A via the rhodamine B-sensitization process by enhancing the production of reactive •O₂⁻ radicals. However, the dye-sensitization mechanism was not observed in the 4-nitrophenol

system owing to the more rapid degradation of rhodamine B than that of 4-nitrophenol. This study offers a simple and novel method to synthesize solid solutions of bismuth-rich oxyhalide materials with the potential for molecular oxygen activation and environmental protection. Other applications, such as H₂ production from water splitting, and removal of heavy metal ions from polluted water, will be further studied in future experiments to extend the utilization of this solid-solution photocatalyst.

Acknowledgements

This research project is supported by Fundamental Fund 2023, Chiang Mai University, and funded by National Research Council of Thailand (NRCT) and Chiang Mai University : N42A650311. Tawanwit Luangwanta would like to thank the Institute for the Promotion of Teaching Science and Technology (IPST). Burapat Inceesungvorn would like to thank Kurita Asia Research Grant (21Pth001-33R) provided by Kurita Water and Environment Foundation.

CRedit authorship contribution statement

Auttaphon Chachvalvutikul: Conceptualization; Methodology; Formal analysis; Investigation; Writing – Original draft; Visualization. **Tawanwit Luangwanta:** Formal analysis; Visualization. **Burapat Inceesungvorn:** Resource. **Sulawan Kaowphong:** Conceptualization; Methodology; Formal analysis; Validation; Investigation; Resources; Writing – review & editing; Visualization; Supervision; Project administration; Funding acquisition.

Declaration of competing interest

The authors declare that there are no conflicts of interest.

References

- [1] W.W. Anku, M.A. Mamo, P.P. Govender, Phenolic compounds in water: sources, reactivity, toxicity and treatment methods, InTechOpen, 2017. <https://doi.org/10.5772/66927>.
- [2] V. Augugliaro, M.J. López-Muñoz, L. Palmisano, J. Soria, Influence of pH on the degradation kinetics of nitrophenol isomers in a heterogeneous photocatalytic system, *Appl. Catal. A Gen.* 101 (1993) 7–13. [https://doi.org/10.1016/0926-860X\(93\)80133-B](https://doi.org/10.1016/0926-860X(93)80133-B).
- [3] A. Di Paola, V. Augugliaro, L. Palmisano, G. Pantaleo, E. Savinov, Heterogeneous photocatalytic degradation of nitrophenols, *J. Photochem. Photobiol. A Chem.* 155 (2003) 207–214. [https://doi.org/10.1016/S1010-6030\(02\)00390-8](https://doi.org/10.1016/S1010-6030(02)00390-8).
- [4] S.F. Yang, C.G. Niu, D.W. Huang, H. Zhang, C. Liang, G.M. Zeng, SrTiO₃ nanocubes decorated with Ag/AgCl nanoparticles as photocatalysts with enhanced visible-light photocatalytic activity towards the degradation of dyes, phenol and bisphenol A, *Environ. Sci. Nano.* 4 (2017) 585–595. <https://doi.org/10.1039/c6en00597g>.
- [5] C.M. Teh, A.R. Mohamed, Roles of titanium dioxide and ion-doped titanium dioxide on photocatalytic degradation of organic pollutants (phenolic compounds and dyes) in aqueous solutions: A review, *J. Alloys Compd.* 509 (2011) 1648–1660. <https://doi.org/10.1016/j.jallcom.2010.10.181>.
- [6] T. Das, P.K. Boruah, M.R. Das, B.K. Saikia, Formation of onion-like fullerene and chemically converted graphene-like nanosheets from low-quality coals: Application in photocatalytic degradation of 2-nitrophenol, *RSC Adv.* 6 (2016) 35177–35190. <https://doi.org/10.1039/c6ra04392e>.

- [7] F. Basheer, I.H. Farooqi, Biodegradation of m-cresol by aerobic granules in a sequencing batch reactor, *Environ. Sci. Technol.* 33 (2012) 1847–1856. <https://doi.org/10.1080/09593330.2011.650218>.
- [8] L. Yang, S. Luo, Y. Li, Y. Xiao, Q. Kang, Q. Cai, High efficient photocatalytic degradation of p-nitrophenol on a unique $\text{Cu}_2\text{O}/\text{TiO}_2$ p-n heterojunction network catalyst, *Environ. Sci. Technol.* 44 (2010) 7641–7646. <https://doi.org/10.1021/es101711k>.
- [9] M. Buser, K. Haire, N. Roney, R. Klein, R. Balachandran, H. Derrick, S. Hall, A. Gao, Toxicological profile for nitrophenols, 2022.
- [10] USEPA, 4-nitrophenol, Health and environmental effects profile No. 135, Washington, DC, 1999.
- [11] A. Careghini, A.F. Mastorgio, S. Saponaro, E. Sezenna, Bisphenol A, nonylphenols, benzophenones, and benzotriazoles in soils, groundwater, surface water, sediments, and food: a review, *Environ. Sci. Pollut. Res.* 22 (2015) 5711–5741. <https://doi.org/10.1007/s11356-014-3974-5>.
- [12] S. Lu, J. Li, F. Duan, L. Duan, M. Du, M. Chen, One-step preparation of $\text{Bi}_4\text{O}_5\text{Br}_x\text{I}_{2-x}$ solid solution with superior photocatalytic performance for organic pollutants degradation under visible light, *Appl. Surf. Sci.* 475 (2019) 577–586. <https://doi.org/10.1016/j.apsusc.2019.01.043>.
- [13] M. Misra, S.R. Chowdhury, T. Il Lee, Sunlight driven decomposition of toxic organic compound, coumarin, p-nitrophenol, and photo reduction of Cr(VI) ions, using a bridge structure of $\text{Au}@\text{CNT}@\text{TiO}_2$ nanocomposite, *Appl. Catal. B Environ.* 272 (2020) 118991. <https://doi.org/10.1016/j.apcatb.2020.118991>.
- [14] T. Jiang, J. Li, Y. Gao, L. Li, T. Lu, L. Pan, BiOBr/BiOF composites for efficient

- degradation of rhodamine B and nitrobenzene under visible light irradiation, *J. Colloid Interface Sci.* 490 (2017) 812–818. <https://doi.org/10.1016/j.jcis.2016.12.007>.
- [15] J. Di, J. Xia, H. Li, S. Guo, S. Dai, Bismuth oxyhalide layered materials for energy and environmental applications, *Nano Energy.* 41 (2017) 172–192. <https://doi.org/10.1016/j.nanoen.2017.09.008>.
- [16] X. Jin, L. Ye, H. Xie, G. Chen, Bismuth-rich bismuth oxyhalides for environmental and energy photocatalysis, *Coord. Chem. Rev.* 349 (2017). <https://doi.org/10.1016/j.ccr.2017.08.010>.
- [17] Y. Bai, L. Ye, T. Chen, P. Wang, L. Wang, X. Shi, P.K. Wong, Synthesis of hierarchical bismuth-rich $\text{Bi}_4\text{O}_5\text{Br}_x\text{I}_{2-x}$ solid solutions for enhanced photocatalytic activities of CO_2 conversion and Cr(VI) reduction under visible light, *Appl. Catal. B Environ.* 203 (2017) 633–640. <https://doi.org/10.1016/j.apcatb.2016.10.066>.
- [18] Q.C. Liu, D.K. Ma, Y.Y. Hu, Y.W. Zeng, S.M. Huang, Various bismuth oxyiodide hierarchical architectures: Alcohothermal-controlled synthesis, photocatalytic activities, and adsorption capabilities for phosphate in water, *ACS Appl. Mater. Interfaces.* 5 (2013) 11927–11934. <https://doi.org/10.1021/am4036702>.
- [19] X. Xiao, W. De Zhang, Hierarchical $\text{Bi}_7\text{O}_9\text{I}_3$ micro/nano- architecture: Facile synthesis, growth mechanism, and high visible light photocatalytic performance, *RSC Adv.* 1 (2011) 1099–1105. <https://doi.org/10.1039/c1ra00323b>.
- [20] R. He, S. Cao, J. Yu, Y. Yang, Microwave-assisted solvothermal synthesis of $\text{Bi}_4\text{O}_5\text{I}_2$ hierarchical architectures with high photocatalytic performance, *Catal. Today.* 264 (2016) 221–228. <https://doi.org/10.1016/j.cattod.2015.07.029>.
- [21] X. Xiao, C. Xing, G. He, X. Zuo, J. Nan, L. Wang, Solvothermal synthesis of novel

- hierarchical Bi₄O₅I₂ nanoflakes with highly visible light photocatalytic performance for the degradation of 4-tert-butylphenol, *Appl. Catal. B Environ.* 148–149 (2014) 154–163. <https://doi.org/10.1016/j.apcatb.2013.10.055>.
- [22] D. Mao, S. Ding, L. Meng, Y. Dai, C. Sun, S. Yang, H. He, One-pot microemulsion-mediated synthesis of Bi-rich Bi₄O₅Br₂ with controllable morphologies and excellent visible-light photocatalytic removal of pollutants, *Appl. Catal. B Environ.* 207 (2017) 153–165. <https://doi.org/10.1016/j.apcatb.2017.02.010>.
- [23] G. Wu, Y. Zhao, Y. Li, B. Souvanhthong, H. Ma, J. Zhao, Facile aqueous synthesis of Bi₄O₅Br₂ nanosheets for improved visible-light photocatalytic activity, *Ceram. Int.* 44 (2018) 5392–5401. <https://doi.org/10.1016/j.ceramint.2017.12.168>.
- [24] J. Xia, Y. Ge, J. Di, L. Xu, S. Yin, Z. Chen, P. Liu, H. Li, Ionic liquid-assisted strategy for bismuth-rich bismuth oxybromides nanosheets with superior visible light-driven photocatalytic removal of bisphenol-A, *J. Colloid Interface Sci.* 473 (2016) 112–119. <https://doi.org/10.1016/j.jcis.2016.03.046>.
- [25] Y. Mi, H. Li, Y. Zhang, W. Hou, Synthesis of belt-like bismuth-rich bismuth oxybromide hierarchical nanostructures with high photocatalytic activities, 2019. <https://doi.org/10.1016/j.jcis.2018.09.038>.
- [26] R. Li, F. Xie, J. Liu, Y. Wang, Y. Wang, X. Zhang, C. Fan, Synthesis of Bi₄O₅Br₂ from reorganization of BiOBr and its excellent visible light photocatalytic activity, *Dalt. Trans.* 45 (2016) 9182–9186. <https://doi.org/10.1039/c6dt00997b>.
- [27] F. Deng, Y. Luo, H. Li, B. Xia, X. Luo, S. Luo, D.D. Dionysiou, Efficient toxicity elimination of aqueous Cr(VI) by positively-charged BiOCl_xI_{1-x}, BiOBr_xI_{1-x} and BiOCl_xBr_{1-x} solid solution with internal hole-scavenging capacity via the synergy of adsorption and

- photocatalytic reduction, *J. Hazard. Mater.* 383 (2020) 121127.
<https://doi.org/10.1016/j.jhazmat.2019.121127>.
- [28] M. Gao, J. Yang, T. Sun, Z. Zhang, D. Zhang, H. Huang, H. Lin, Y. Fang, X. Wang, Persian buttercup-like BiOBr_xCl_{1-x} solid solution for photocatalytic overall CO₂ reduction to CO and O₂, *Appl. Catal. B Environ.* 243 (2019) 734–740.
<https://doi.org/10.1016/j.apcatb.2018.11.020>.
- [29] M. Kou, Y. Deng, R. Zhang, L. Wang, P.K. Wong, F. Su, L. Ye, Molecular oxygen activation enhancement by BiOBr_{0.5}I_{0.5}/BiOI utilizing the synergistic effect of solid solution and heterojunctions for photocatalytic NO removal, *Chinese J. Catal.* 41 (2020) 1480–1487.
[https://doi.org/10.1016/S1872-2067\(20\)63607-5](https://doi.org/10.1016/S1872-2067(20)63607-5).
- [30] N. Mohseni, M. Haghghi, M. Shabani, Sunlight-activated 3D-mesoporous-flowerlike Cl–Br bismuth oxides nanosheet solid solution: In situ EG-thermal-sonication synthesis with excellent photodecomposition of ciprofloxacin, *Environ. Res.* 188 (2020) 109810.
<https://doi.org/10.1016/j.envres.2020.109810>.
- [31] Y. Bai, P. Yang, P. Wang, Z. Fan, H. Xie, P.K. Wong, L. Ye, Solid phase fabrication of Bismuth-rich Bi₃O₄Cl_xBr_{1-x} solid solution for enhanced photocatalytic NO removal under visible light, *J. Taiwan Inst. Chem. Eng.* 82 (2018) 273–280.
<https://doi.org/10.1016/j.jtice.2017.10.021>.
- [32] Y. Bai, X. Shi, P. Wang, L. Wang, H. Xie, Z. Li, L. Qu, L. Ye, Synthesis of one-dimensional Bi₅O₇Br_{0.5}I_{0.5} solid solution for effective real oilfield wastewater treatment via exciton photocatalytic process, *J. Taiwan Inst. Chem. Eng.* 91 (2018) 358–368.
<https://doi.org/10.1016/j.jtice.2018.05.045>.
- [33] D. Zhang, F. Wang, S. Cao, X. Duan, Rapid microwave irradiation synthesis and

- characterization of $\text{Bi}_7\text{O}_9\text{I}_3$ photocatalyst for the degradation of bisphenol A, *Mater. Lett.* 218 (2018) 32–35. <https://doi.org/10.1016/j.matlet.2018.01.105>.
- [34] F. Chang, C. Yang, J. Wang, B. Lei, S. Li, H. Kim, Enhanced photocatalytic conversion of NO_x with satisfactory selectivity of 3D-2D $\text{Bi}_4\text{O}_5\text{Br}_2$ -GO hierarchical structures via a facile microwave-assisted preparation, *Sep. Purif. Technol.* 266 (2021) 118237. <https://doi.org/10.1016/j.seppur.2020.118237>.
- [35] X. Xiao, R. Hao, X. Zuo, J. Nan, L. Li, W. Zhang, Microwave-assisted synthesis of hierarchical $\text{Bi}_7\text{O}_9\text{I}_3$ microsheets for efficient photocatalytic degradation of bisphenol-A under visible light irradiation, *Chem. Eng. J.* 209 (2012) 293–300. <https://doi.org/10.1016/j.cej.2012.07.142>.
- [36] Y.J. Zhu, F. Chen, Microwave-assisted preparation of inorganic nanostructures in liquid phase, *Chem. Rev.* 114 (2014) 6462–6555. <https://doi.org/10.1021/cr400366s>.
- [37] A. Chachvalvutikul, S. Kaowphong, Direct Z-scheme $\text{FeVO}_4/\text{BiOCl}$ heterojunction as a highly efficient visible-light-driven photocatalyst for photocatalytic dye degradation and Cr(VI) reduction, *Nanotechnology.* 31 (2020). <https://doi.org/10.1088/1361-6528/ab61d1>.
- [38] S. Kaowphong, T. Luangwanta, A. Chachvalvutikul, Facile synthesis and enhanced photocatalytic activity of a novel $\text{FeVO}_4/\text{Bi}_4\text{O}_5\text{Br}_2$ heterojunction photocatalyst through step-scheme charge transfer mechanism, *Colloids Surfaces A Physicochem. Eng. Asp.* 627 (2021) 127217. <https://doi.org/10.1016/j.colsurfa.2021.127217>.
- [39] C.L. Hsu, C.W. Lien, S.G. Harroun, R. Ravindranath, H.T. Chang, J.Y. Mao, C.C. Huang, Metal-deposited bismuth oxyiodide nanonetworks with tunable enzyme-like activity: Sensing of mercury and lead ions, *Mater. Chem. Front.* 1 (2017) 893–899. <https://doi.org/10.1039/c6qm00149a>.

- [40] W. Zhang, G. Li, W. Wang, Y. Qin, T. An, X. Xiao, W. Choi, Enhanced photocatalytic mechanism of Ag_3PO_4 nano-sheets using MS_2 ($\text{M} = \text{Mo}, \text{W}$)/rGO hybrids as co-catalysts for 4-nitrophenol degradation in water, *Appl. Catal. B Environ.* 232 (2018) 11–18. <https://doi.org/10.1016/j.apcatb.2018.03.006>.
- [41] A. Chachvalvutikul, T. Luangwanta, S. Kaowphong, Double Z-scheme $\text{FeVO}_4/\text{Bi}_4\text{O}_5\text{Br}_2/\text{BiOBr}$ ternary heterojunction photocatalyst for simultaneous photocatalytic removal of hexavalent chromium and rhodamine B, *J. Colloid Interface Sci.* 603 (2021) 738–757. <https://doi.org/10.1016/j.jcis.2021.06.124>.
- [42] Y. Bai, X. Shi, P. Wang, L. Wnag, K. Zhang, Y. Zhou, H. Xie, J. Wang, L. Ye, $\text{BiOBr}_x\text{I}_{1-x}/\text{BiOBr}$ heterostructure engineering for efficient molecular oxygen activation, *Chem. Eng. J.* 356 (2019) 34–42. <https://doi.org/10.1016/j.cej.2018.09.006>.
- [43] J.C. Wang, J. Ren, H.C. Yao, L. Zhang, J.S. Wang, S.Q. Zang, L.F. Han, Z.J. Li, Synergistic photocatalysis of Cr(VI) reduction and 4-Chlorophenol degradation over hydroxylated $\alpha\text{-Fe}_2\text{O}_3$ under visible light irradiation, *J. Hazard. Mater.* 311 (2016) 11–19. <https://doi.org/10.1016/j.jhazmat.2016.02.055>.
- [44] O.C. Compton, F.E. Osterloh, Niobate nanosheets as catalysts for photochemical water splitting into hydrogen and hydrogen peroxide, *J. Phys. Chem. C.* 113 (2009) 479–485. <https://doi.org/10.1021/jp807839b>.
- [45] C. Zeng, Y. Hu, H. Huang, $\text{BiOBr}_{0.75}\text{I}_{0.25}/\text{BiOIO}_3$ as a Novel Heterojunctional photocatalyst with superior visible-light-driven photocatalytic activity in removing diverse industrial pollutants, *ACS Sustain. Chem. Eng.* 5 (2017) 3897–3905. <https://doi.org/10.1021/acssuschemeng.6b03066>.
- [46] A. Chachvalvutikul, J. Jakmune, S. Thongtem, S. Kittiwachana, S. Kaowphong, Novel

- FeVO₄/Bi₇O₉I₃ nanocomposite with enhanced photocatalytic dye degradation and photoelectrochemical properties, *Appl. Surf. Sci.* 475 (2019) 175–184. <https://doi.org/10.1016/j.apsusc.2018.12.214>.
- [47] X. Xiao, W.-D. Zhang, Hierarchical Bi₇O₉I₃ micro/nano-architecture: facile synthesis, growth mechanism, and high visible light photocatalytic performance, *RSC Adv.* 1 (2011) 1099. <https://doi.org/10.1039/c1ra00323b>.
- [48] S.G. Fard, M. Haghghi, M. Shabani, Facile one-pot ultrasound-assisted solvothermal fabrication of ball-flowerlike nanostructured (BiOBr)_x(Bi₇O₉I₃)_{1-x} solid-solution for high active photodegradation of antibiotic levofloxacin under sun-light, *Appl. Catal. B Environ.* 248 (2019) 320–331. <https://doi.org/10.1016/j.apcatb.2019.02.021>.
- [49] M. Long, P. Hu, H. Wu, Y. Chen, B. Tan, W. Cai, Understanding the composition and electronic structure dependent photocatalytic performance of bismuth oxyiodides, *J. Mater. Chem. A.* 3 (2015) 5592–5598. <https://doi.org/10.1039/c4ta06134a>.
- [50] X. Xiao, M. Lu, J. Nan, X. Zuo, W. Zhang, S. Liu, S. Wang, Rapid microwave synthesis of I-doped Bi₄O₅Br₂ with significantly enhanced visible-light photocatalysis for degradation of multiple parabens, *Appl. Catal. B Environ.* 218 (2017) 398–408. <https://doi.org/10.1016/j.apcatb.2017.06.074>.
- [51] Q. Wang, Z. Liu, D. Liu, G. Liu, M. Yang, F. Cui, W. Wang, Ultrathin two-dimensional BiOBr_xI_{1-x} solid solution with rich oxygen vacancies for enhanced visible-light-driven photoactivity in environmental remediation, *Appl. Catal. B Environ.* 236 (2018) 222–232. <https://doi.org/10.1016/j.apcatb.2018.05.029>.
- [52] Z. Jia, F. Wang, F. Xin, B. Zhang, Simple solvothermal routes to synthesize 3D BiOBr_xI_{1-x} microspheres and their visible-light-induced photocatalytic properties, *Ind. Eng. Chem.*

- Res. 50 (2011) 6688–6694. <https://doi.org/10.1021/ie102310a>.
- [53] R. Li, J. Liu, X. Zhang, Y. Wang, Y. Wang, C. Zhang, X. Zhang, C. Fan, Iodide-modified Bi₄O₅Br₂ photocatalyst with tunable conduction band position for efficient visible-light decontamination of pollutants, *Chem. Eng. J.* 339 (2018) 42–50. <https://doi.org/10.1016/j.cej.2018.01.109>.
- [54] H. Wang, D. Yong, S. Chen, S. Jiang, X. Zhang, W. Shao, Q. Zhang, W. Yan, B. Pan, Y. Xie, Oxygen-vacancy-mediated exciton dissociation in biobr for boosting charge-carrier-involved molecular oxygen activation, *J. Am. Chem. Soc.* 140 (2018) 1760–1766. <https://doi.org/10.1021/jacs.7b10997>.
- [55] S. Uhlenbrock, C. Scharfschwerdt, M. Neumann, G. Illing, H.J. Freund, The influence of defects on the Ni 2p and O 1s XPS of NiO, *J. Phys. Condens. Matter.* 4 (1992) 7973–7978. <https://doi.org/10.1088/0953-8984/4/40/009>.
- [56] X. Lv, D.Y.S. Yan, F. L.-Y. Lam, Y. Hau Ng, S. Yin, A. Kyoungjin An, Solvothermal synthesis of copper-doped BiOBr microflowers with enhanced adsorption and visible-light driven photocatalytic degradation of norfloxacin, *Chem. Eng. J.* 401 (2020) 126012. <https://doi.org/10.1016/j.cej.2020.126012>.
- [57] M. Jiang, Y. Shi, J. Huang, L. Wang, H. She, J. Tong, B. Su, Q. Wang, Synthesis of Flowerlike g-C₃N₄/BiOBr with Enhanced Visible Light Photocatalytic Activity for Dye Degradation, *Eur. J. Inorg. Chem.* 2018 (2018) 1834–1841. <https://doi.org/10.1002/ejic.201800110>.
- [58] J. Hu, C. Zhai, C. Yu, L. Zeng, Z.-Q. Liu, M. Zhu, Visible light-enhanced electrocatalytic alcohol oxidation based on two dimensional Pt-BiOBr nanocomposite, *J. Colloid Interface Sci.* 524 (2018) 195–203. <https://doi.org/10.1016/j.jcis.2018.03.104>.

- [59] B. Zhang, H. Zhang, Z. Wang, X. Zhang, X. Qin, Y. Dai, Y. Liu, P. Wang, Y. Li, B. Huang, Doping strategy to promote the charge separation in BiVO₄ photoanodes, *Appl. Catal. B Environ.* 211 (2017) 258–265. <https://doi.org/10.1016/j.apcatb.2017.03.078>.
- [60] S. Kaowphong, W. Choklap, A. Chachvalvutikul, N. Chandet, A novel CuInS₂/m-BiVO₄ p-n heterojunction photocatalyst with enhanced visible-light photocatalytic activity, *Colloids Surfaces A Physicochem. Eng. Asp.* 579 (2019) 123639. <https://doi.org/10.1016/j.colsurfa.2019.123639>.
- [61] F.A. Carey, *Organic Chemistry*, 4th ed., McGraw-Hill Higher Education, 2000.
- [62] K. Tanaka, W. Luesaiwong, T. Hisanaga, Photocatalytic degradation of mono-, di- and trinitrophenol in aqueous TiO₂ suspension, *J. Mol. Catal. A Chem.* 122 (1997) 67–74. [https://doi.org/10.1016/S1381-1169\(96\)00509-2](https://doi.org/10.1016/S1381-1169(96)00509-2).
- [63] V. Augugliaro, L. Palmisano, M. Schiavello, Photocatalytic degradation of nitrophenols in aqueous titanium dioxide dispersion, *Appl. Catal.* 69 (1991) 323–340. [https://doi.org/10.1016/S0166-9834\(00\)83310-2](https://doi.org/10.1016/S0166-9834(00)83310-2).
- [64] M.S. Dieckmann, K.A. Gray, P. V. Kamat, Photocatalyzed degradation of adsorbed nitrophenolic compounds on semiconductor surfaces, *Water Sci. Technol.* 25 (1992) 277–279. <https://doi.org/10.2166/wst.1992.0106>.
- [65] C. Moreno-Castilla, M.V. López-Ramón, M. ángeles Fontecha-Cámara, M.A. Álvarez, L. Mateus, Removal of phenolic compounds from water using copper ferrite nanosphere composites as fenton catalysts, *Nanomaterials.* 9 (2019). <https://doi.org/10.3390/nano9060901>.
- [66] Y. Jia, Y. Yang, W. Guo, Q. Qin, X. Yang, Y. Guo, Y. Guo, Simulated sunlight photocatalytic degradation of aqueous p-nitrophenol and bisphenol A in a Pt/BiOBr film-

- coated quartz fiber photoreactor, *Dalt. Trans.* 44 (2015) 9439–9449. <https://doi.org/10.1039/c5dt00417a>.
- [67] W. Guo, Y. Yang, Y. Guo, Y. Jia, H. Liu, Y. Guo, Self-assembled hierarchical $\text{Bi}_{12}\text{TiO}_{20}$ /graphene nanoarchitectures with excellent simulated sunlight photocatalytic activity, *Phys. Chem. Chem. Phys.* 16 (2014) 2075. <https://doi.org/10.1039/c3cp53070a>.
- [68] L. Zhang, W. Wang, S. Sun, Y. Sun, E. Gao, Z. Zhang, Elimination of BPA endocrine disruptor by magnetic $\text{BiOBr@SiO}_2\text{@Fe}_3\text{O}_4$ photocatalyst, *Appl. Catal. B Environ.* 148–149 (2014) 164–169. <https://doi.org/10.1016/j.apcatb.2013.10.053>.
- [69] Z. Liu, H. Ran, J. Niu, P. Feng, Y. Zhu, One-pot synthesis of bismuth oxyhalide/oxygen-rich bismuth oxyhalide heterojunction and its photocatalytic activity, *J. Colloid Interface Sci.* 431 (2014) 187–193. <https://doi.org/10.1016/j.jcis.2014.06.020>.
- [70] Z. Liu, J. Niu, P. Feng, Y. Zhu, Solvothermal synthesis of $\text{Bi}_{24}\text{O}_{31}\text{Cl}_x\text{Br}_{10-x}$ solid solutions with enhanced visible light photocatalytic property, *Ceram. Int.* 41 (2015) 4608–4615. <https://doi.org/10.1016/j.ceramint.2014.12.004>.
- [71] W. Bin Zhang, X. Xiao, Q.F. Wu, Q. Fan, S. Chen, W.X. Yang, F.C. Zhang, Facile synthesis of novel Mn-doped $\text{Bi}_4\text{O}_5\text{Br}_2$ for enhanced photocatalytic NO removal activity, *J. Alloys Compd.* 826 (2020) 154204. <https://doi.org/10.1016/j.jallcom.2020.154204>.
- [72] H. Li, F. Ren, J. Liu, Q. Wang, Q. Li, J. Yang, Y. Wang, Endowing single-electron-trapped oxygen vacancy self-modified titanium dioxide with visible-light photocatalytic activity by grafting Fe(III) nanocluster, *Appl. Catal. B Environ.* 172–173 (2015) 37–45. <https://doi.org/10.1016/j.apcatb.2015.02.008>.
- [73] X. Zhao, Y. You, S. Huang, Y. Wu, Y. Ma, G. Zhang, Z. Zhang, Z-scheme photocatalytic production of hydrogen peroxide over $\text{Bi}_4\text{O}_5\text{Br}_2/\text{g-C}_3\text{N}_4$ heterostructure under visible light,

- Appl. Catal. B Environ. (2020) 119251. <https://doi.org/10.1016/j.apcatb.2020.119251>.
- [74] J. Liu, Y. Zhang, L. Lu, G. Wu, W. Chen, Self-regenerated solar-driven photocatalytic water-splitting by urea derived graphitic carbon nitride with platinum nanoparticles, Chem. Commun. 48 (2012) 8826–8828. <https://doi.org/10.1039/c2cc33644h>.
- [75] L. Wang, S. Cao, K. Guo, Z. Wu, Z. Ma, L. Piao, Simultaneous hydrogen and peroxide production by photocatalytic water splitting, Chinese J. Catal. 40 (2019) 470–475. [https://doi.org/10.1016/s1872-2067\(19\)63274-2](https://doi.org/10.1016/s1872-2067(19)63274-2).
- [76] H. Li, F. Deng, Y. Zheng, L. Hua, C. Qu, X. Luo, Visible-light-driven Z-scheme rGO/Bi₂S₃–BiOBr heterojunctions with tunable exposed BiOBr (102) facets for efficient synchronous photocatalytic degradation of 2-nitrophenol and Cr(vi) reduction, Environ. Sci. Nano. 6 (2019) 3670–3683. <https://doi.org/10.1039/c9en00957d>.
- [77] L. Han, Y. Lv, B. Li, H. Wen, H. Huang, Y. Guo, Z. Lin, Enhancing H₂ evolution and molecular oxygen activation via dye sensitized BiOBr_{0.9}I_{0.1} under visible light, J. Colloid Interface Sci. (2020) 0–25. <https://doi.org/10.1016/j.jcis.2020.07.014>.
- [78] L. Yu, X. Zhang, G. Li, Y. Cao, Y. Shao, D. Li, Highly efficient Bi₂O₂CO₃/BiOCl photocatalyst based on heterojunction with enhanced dye-sensitization under visible light, Appl. Catal. B Environ. 187 (2016) 301–309. <https://doi.org/10.1016/j.apcatb.2016.01.045>.
- [79] A. Baral, D.P. Das, M. Minakshi, M.K. Ghosh, D.K. Padhi, Probing environmental remediation of RhB organic dye using α -MnO₂ under visible- light irradiation: structural, photocatalytic and mineralization studies, ChemistrySelect. 1 (2016) 4277–4285. <https://doi.org/10.1002/slct.201600867>.